The Astrophysical Journal, 892:34 (19pp), 2020 March 20 https://doi.org/10.3847/1538-4357/ab7924

Stellar-mass Measurements in A133 with Magellan/IMACS

S. Starikova[1], A. Vikhlinin[1], A. Kravtsov[2], R. Kraft[1], T. Connor[3,4], J. S. Mulchaey[3], and D. Nagai[5,6,7]
[1] Center for Astrophysics | Harvard & Smithsonian, 60 Garden Street, Cambridge, MA 02138, USA; svetlana.starikova@cfa.harvard.edu, avikhlinin@cfa.harvard.edu
[2] Department of Astronomy & Astrophysics, Kavli Institute for Cosmological Physics, Enrico Fermi Institute, The University of Chicago, Chicago, IL 60637, USA
[3] The Observatories of the Carnegie Institution for Science, 813 Santa Barbara Street, Pasadena, CA 91101, USA
[4] Jet Propulsion Laboratory, California Institute of Technology, 4800 Oak Grove Drive, Pasadena, CA 91109, USA
[5] Department of Physics, Yale University, New Haven, CT 06520, USA
[6] Department of Astronomy, Yale University, New Haven, CT 06520, USA
[7] Yale Center for Astronomy & Astrophysics, Yale University, New Haven, CT 06520, USA
Received 2019 October 11; revised 2020 January 17; accepted 2020 February 20; published 2020 March 24

Abstract

We present the analysis of deep optical imaging of the galaxy cluster A133 with the IMACS instrument on Magellan. Our multi-band photometry enables stellar-mass measurements in the cluster member galaxies down to a mass limit of $M_\star = 3 \times 10^8\,M_\odot$ (≈0.1 of the Large Magellanic Cloud stellar mass). We observe a clear difference in the spatial distribution of large and dwarf galaxies within the cluster. Modeling these galaxy populations separately, we can confidently track the distribution of stellar mass locked in the galaxies to the cluster's virial radius. The extended envelope of the cluster's brightest galaxy can be tracked to ∼200 kpc. The central galaxy contributes ∼1/3 of the total cluster stellar mass within the radius r_{500c}.

Unified Astronomy Thesaurus concepts: Galaxy clusters (584); Photometry (1234); Stellar mass functions (1612); Galaxies (573)

1. Introduction

Clusters of galaxies have total gravitating masses of $\sim 10^{14}$–$10^{15}\,M_\odot$ and are the most massive systems that have had time to collapse in the standard ΛCDM cosmology (see Kravtsov & Borgani 2012, for a review). Given a mean comoving density of matter in the universe of $\approx 4 \times 10^{10}\,M_\odot\,\mathrm{Mpc}^{-3}$, the large cluster masses imply that their matter was assembled from regions of ∼15–50 Mpc in size. Although clusters tend to form in high-density regions (Kaiser 1984), the vast scales involved in their formation mean that, at least within roughly the virial radius, the enclosed matter should have a mix of baryons and dark matter close to the universal value (e.g., White et al. 1993; Frenk et al. 1999; Valdarnini 2003; Kay et al. 2004; Kravtsov et al. 2005). Furthermore, the sizes of their virialized regions after collapse are $R \sim$ 1–5 Mpc, and their binding energies, GM^2/R, are thus $\sim 10^{63}$–10^{64} erg. Therefore, even the most energetic Active Galactic Nuclei (AGNs) feedback cannot eject baryons from deep potential wells of clusters and significantly lower their baryon mass fraction (e.g., Battaglia et al. 2013; Planelles et al. 2013; Henden et al. 2018). This means that clusters should be approximately closed systems.

Studies of the total baryon fractions in clusters can thus be used as a valuable test of the overall structure formation paradigm (see, e.g., Allen et al. 2011, for a review). At the same time, baryon mass fractions within the radii readily accessible by current X-ray observations, ∼0.5 of the virial radius, are well below the values of the universal baryon fraction derived from Cosmic Microwave Background fluctuations (Vikhlinin et al. 2006; Lin et al. 2012; Eckert et al. 2016), and this is yet to be fully explained by cosmological cluster simulations (e.g., Barnes et al. 2017). Furthermore, the distribution of stellar material and hot gas within clusters should bear the imprint of key processes shaping galaxy formation. Indeed, observed stellar-mass fractions and stellar-mass function of cluster galaxies have become valuable benchmarks for testing models of feedback in cosmological simulations of cluster formation (e.g., Martizzi et al. 2014, 2016; Bahé et al. 2017; McCarthy et al. 2017; Cui et al. 2018; Henden et al. 2018; Pillepich et al. 2018). The radial profile of stellar density of the Brightest Cluster Galaxy (BCG), as well as the radial distribution of stellar mass in galaxies are potentially equally powerful constraints on the models (e.g., Martizzi et al. 2014; Bellstedt et al. 2018).

Despite recent progress (Budzynski et al. 2012, 2014; Gonzalez et al. 2013; Huang et al. 2018; Kravtsov et al. 2018), the number of clusters with available accurate measurements of the gas mass, stellar mass in galaxies down to dwarf scales, and stellar material in the outer envelope of the central galaxy remains small. The main goal of this study is to accurately measure the contribution of the stellar populations (individual galaxies and intracluster light) to the total baryon budget in the cluster A133.

A133 is a massive nearby ($z = 0.05695$) galaxy cluster with extensive mapping of surrounding distribution of galaxies and filamentary cosmic web structure (Connor et al. 2018, 2019b), as well as deep X-ray observations by the *Chandra* X-ray Observatory (Vikhlinin et al. 2006; Vikhlinin 2013; Morandi & Cui 2014; A. Vikhlinin et al. 2020, in preparation). The cluster has a cool core and prominent radio relics indicative of the ongoing merger activity (Randall et al. 2010), although distribution of galaxies does not reveal clear signs of dynamical disturbance (Connor et al. 2018). Hydrostatic equilibrium analysis using X-ray *Chandra* observations give total mass within the radius enclosing density contrast equal to the 500 times the critical density at the redshift of the cluster of $M_{500c} \approx 3.42 \times 10^{14}\,M_\odot$ and corresponding radius $r_{500c} =$ 1.048 Mpc.

The paper is organized as follows. In Section 2, we explain the choice of fields within A133 and neighboring fields used to estimate background galaxy density, describe observations of these fields using the IMACS camera on the 6.5 m Magellan Baade telescope and present their images and general discussion of the features they reveal.

In Section 3, we describe data reduction procedures, assumptions, and methods we use to carry out source detection, classification, galaxy photometry, and sample completeness. In Section 4, we describe the method we use to estimate stellar masses from galaxy luminosities and colors (Section 4.1) and results pertaining to the stellar-mass function (Section 4.2). In Section 5, we present the radial distribution of galaxies of different stellar mass (Section 5.1), the radial stellar-mass distribution of the BCG (Section 5.2), and the total mass profile of all stars in the cluster (Section 5.3). We discuss our findings and their interpretation in Section 6 and summarize our main results and conclusions in Section 7.

All distant-dependent quantities throughout this paper are computed assuming the nominal best-fit cosmological parameters from Bennett et al. (2014): $h = 0.696$, $\Omega_{\rm M} = 0.286$, and $\Omega_\Lambda = 0.714$. Galaxy luminosities are computed in the rest-frame using the Vega magnitude system.

2. Observations

The galaxy cluster A133 was observed on the 6.5 m Magellan Baade Telescope over three nights in 2005. The observations were performed with the Inamori-Magellan Areal Camera and Spectrograph (IMACS; Dressler et al. 2011), instrument in its $f/2$ focus configuration with the 8192 × 8192 pixel Mosaic1 detector. The central cluster region and southeast extension were covered with a six-location grid (Figure 1). The coverage reaches outside the r_{200c}[8] radius in the west, south, and southwest directions from the cluster center. Unfortunately, the northeast corner of the cluster remained unobserved. In analyzing the galaxy distributions below, we make an assumption of azimuthal symmetry.

Since the fore- and background galaxy populations have to be subtracted statistically in the cluster pointings, we obtained data for their careful calibration. Specifically, we observed eight background fields at $\sim 1\overset{\circ}{.}5$ ($\approx$6 Mpc) distances from the cluster center. Approximately half of all available exposure time was spent in these background fields, so the background images reach the same depth as the A133 pointings. Also, we constantly alternated between the cluster and background fields during the night, so the background pointings can be used for a measurement of the diffuse sky background. This turned out to be crucial for analyzing the extended diffuse light halo of the cluster central galaxy (see Section 5.2 for details). We chose to observe the fields for background estimation at 6 Mpc $\approx 3.5 r_{200c}$, as opposed to using random pointings far away from the cluster, because most of the volume at $z \sim 0$ is in low-density regions. At the same time, galaxies and mass are strongly correlated with clusters, and the average profile of mass around clusters is expected to reach mean density only at $\gtrsim 10 R_{\rm vir}$ (e.g., Diemer & Kravtsov 2014). A significant contribution to the relevant projected background is thus expected to be due to such correlated structures relatively close to the cluster, while commonly used estimates of the background using random fields will underestimate the background (see, e.g., discussion in Section 2.2.3 of Busch & White 2017). Therefore, we chose to estimate background at the radii well outside the virial radius but still sufficiently close to the cluster to give us a realistic estimate of the background population.

All fields were observed in the Bessel V, Bessel R, and CTIO I filters. In each filter, several exposures were taken with $\sim 15''$ dither to facilitate removal of cosmic rays and cosmetic defects of the CCDs. The total exposure per location per filter was in the range from 300 to 1800 s. The deepest images were taken in the R-band (typical exposures $\sim$900 s), while V- and I-band images are shallower (typically, 300 s). The deepest exposures were taken for the central cluster field and one of the background fields—1800, 1500 and 900 s in R, V, and I filters, respectively. Seeing varied during the observing run in the range $0\overset{''}{.}6$–$1\overset{''}{.}2$ but stayed sub-arcsec for a large fraction of the R-band observations. For accurate photometric calibration, we observed the standard star field SA 98 Landolt (1992) in R, V, and I filters in the pre-dawn hours of each night.

When this paper was in preparation, the first release of the Dark Energy Survey (DES; DES Collaboration 2018) data near the A133 location became available. The DES data cover a larger area around the cluster and provide accurate photometry in the SDSS filters. However, we find that the DES images are shallower than our Magellan data (see Figure 3 below). We, therefore, used the DES catalogs to verify the accuracy of photometric measurements and stellar-mass determinations from Magellan data for commonly detected galaxies (see Appendix B).

2.1. General Discussion of Magellan Images

The composite Magellan image (Figure 1) clearly shows a large number of A133 member galaxies. The cluster is dominated by the brightest central galaxy. We show below that the BCG, including its extended envelope, contributes over 30% of the total stellar mass in the cluster within r_{500c} and $\sim$50% within $0.5\,r_{500c}$ (Section 5.3). There are a few other structures worthy of brief discussion.

In Figure 2, we show a zoom-in on the cluster central region. The colors represent the relative flux in the V, R, and I bands, and are chosen such that the color of galaxies on the A133's red sequence is white. In addition to a large number of A133 members, the image clearly shows a concentration of fainter, red galaxies $\sim$150 kpc to the southeast of the BCG. This group of galaxies forms a separate red sequence and corresponds to a background galaxy cluster at $z \approx 0.29$ (see Section 3.4 below).

At a distance of $\sim$300 kpc to the southwest of the BCG, there is a filamentary structure with bluer colors than the A133 elliptical galaxies. This structure possibly corresponds to a tidally disrupted cluster member. It has a size of 100 kpc, apparent magnitude $R = 19.8$ mag, and color $V - R = 0.19$ mag, $\approx$0.3 mag bluer than the A133 red sequence (see Figure 9 below). Other examples of tidally disrupted galaxies in nearby clusters have been reported, such as UGC 6697 in A1367 (Sun & Vikhlinin 2005) and ESO 137-001 in A3627 (Sun et al. 2007). These objects show $\sim$50 kpc tails of Hα and X-ray emission. The filamentary structure in A133 is larger in size and does not show any X-ray tails in the sensitive *Chandra* data (no narrow-band Hα imaging is available at the time of this writing). Further analysis of these structures will require additional data.

[8] $r_{200c} \simeq 1.54 r_{500c}$ assuming concentration parameter indicated by the total mass profile of the cluster derived using hydrostatic equilibrium equation using X-ray data.

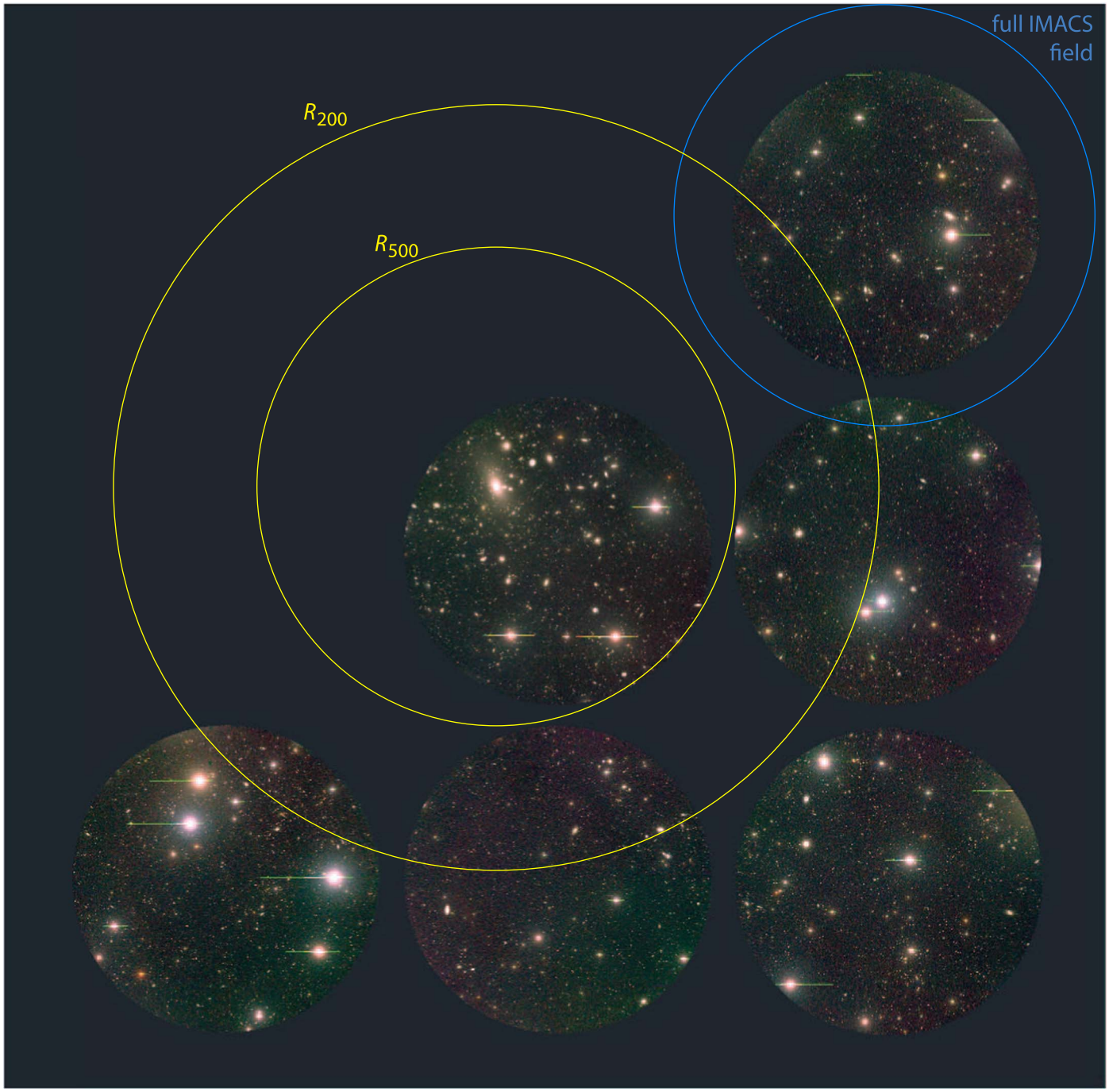

Figure 1. Mosaic of IMACS observations of A133, blending the images in the *R*, *V*, and *I* filters. Only the inner 20′ diameter regions of each field were used in the analysis (Section 3.2) and are shown here. The full IMACS field of view (27.′4 diameter) is shown by the blue circle for guidance. Yellow circles mark r_{500c} and r_{200c} radii of the cluster. Note that all data shown in this image are the "cluster" fields. We have obtained an additional set of eight background fields (not shown here) at ∼1.°5 off-cluster distances.

3. Data Analysis

3.1. Basic Image Reduction

Basic data reduction steps including bias removal, dark current correction, and flat-fielding using twilight flats were performed with IRAF's CCDPROC package. Individual images in each dither pattern were merged using a combination of mean and median averaging with sigma-clipping. This procedure automatically removes the cosmic rays and cosmetic CCD defects.

The astrometric solutions were obtained using the *Astrometry.net* package (Lang et al. 2010). All images were then resampled to a common tangential projections. This step was necessary for accurate matching of the images obtained in individual filters and for creating large-scale mosaics such as those shown in Figure 1. Because the IMACS $f/2$ camera was slightly misaligned prior to adjustments made in 2006 and 2008,[9] resampling to a global tangential projection resulted in small aliasing effects. Those effects have not seriously affected the image quality because the image pixel size, 0.″2, is

[9] http://www.lco.cl/telescopes-information/magellan/instruments/imacs/user-manual/the-imacs-user-manual

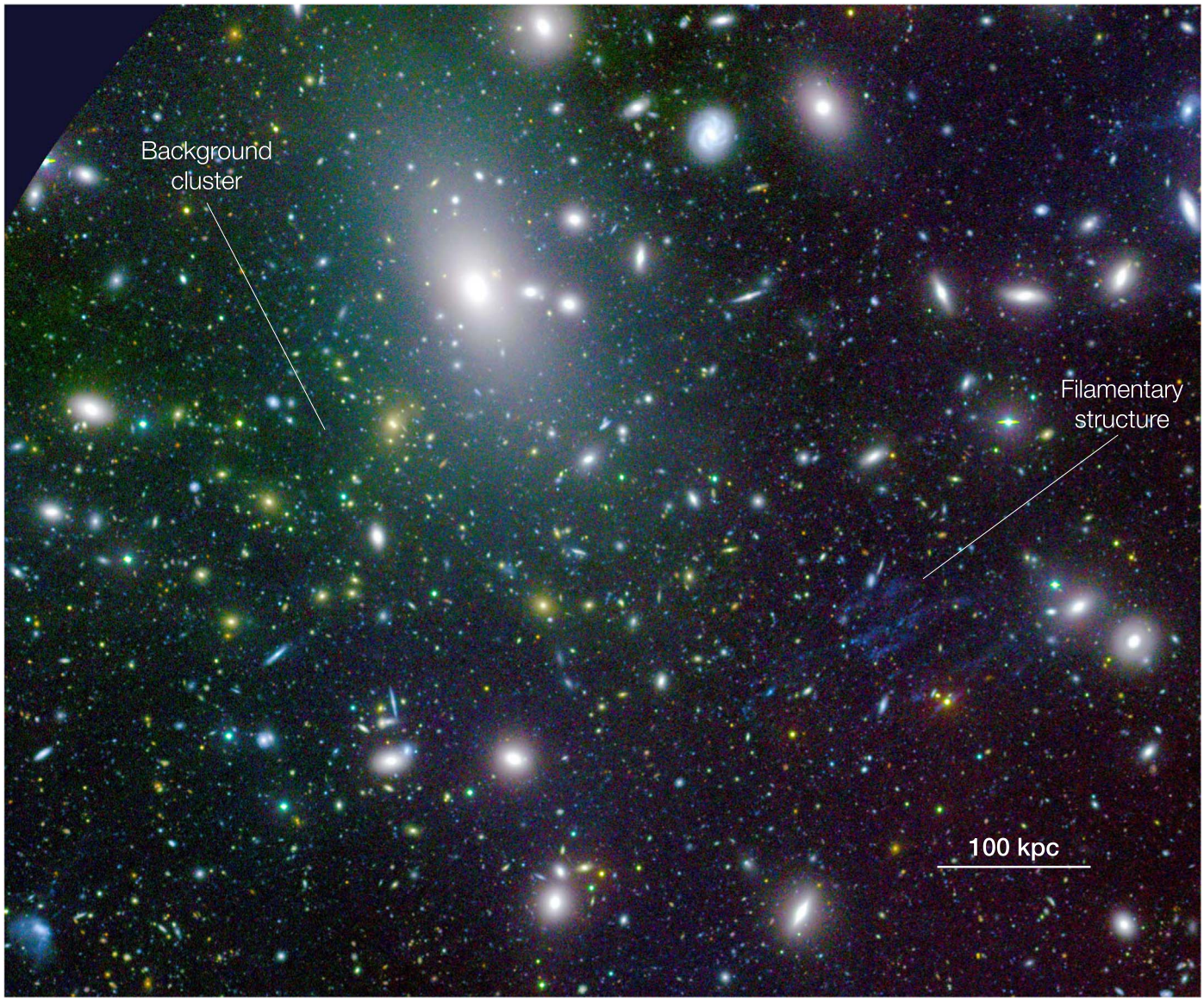

Figure 2. Zoom-in on the central region of A133. North is up, east is to the left, and the colors in the *V*, *R*, and *I* blend are chosen so that the A133 red sequence corresponds to white. Approximately ∼300 kpc southwest of the BCG, there is a filamentary structure with bluer colors than the population of A133 ellipticals. Approximately 150 kpc to the southeast of the A133 BCG, there lies a projected background cluster ($z = 0.29$), apparent as a group of redder galaxies (Section 3.4).

substantially smaller than the seeing during the A133 observing run. However, aliasing modifies the pixel-to-pixel noise in the final images and has to be taken into account during object detection (see Section 3.3.1 and Appendix A below).

3.2. Background Subtraction

To accurately calculate fluxes of bright and faint sources, we use global and local background subtraction methods. Sky brightness and noise levels heavily varied among images of the same exposure in a given field. However, we noticed that for every image, there was a linear dependence between sky brightnesses in the center and the center-to-edge difference. This dependence was exploited to remove the time variations of the background. Therefore, we could build a combined background image from all observed background fields taking into account individual levels of noise and sky, and excluding point sources. This image, the global background pattern, was subtracted from all observations. Unfortunately, using this method, we could not model random spatial variations of the background, which appear in some fields. We applied the local background subtraction method to produce images that we used for detection and flux measurements for the majority of sources (see Appendix A for a description of this procedure).

Individually processed images were combined into the final master images for every cluster and background field. The IMACS CCD camera ideally delivers a 27.′4 diameter field. However, there was substantial loss of image quality (coma and astigmatism) near the edge of the field of view prior to 2008, in addition to substantial vignetting. We also found that the background pattern near the field edge was unrepeatable, which was problematic for global background subtraction. Therefore, we reduced the diameters of our fields to 20′.

The bright, saturated stars render a portion of the cluster field unusable for detection of faint sources and accurate galaxy photometry. We masked out such regions (∼40″ radius) and excluded them from all further analysis. This excludes ∼3% of the overall image area. More extended wings around bright

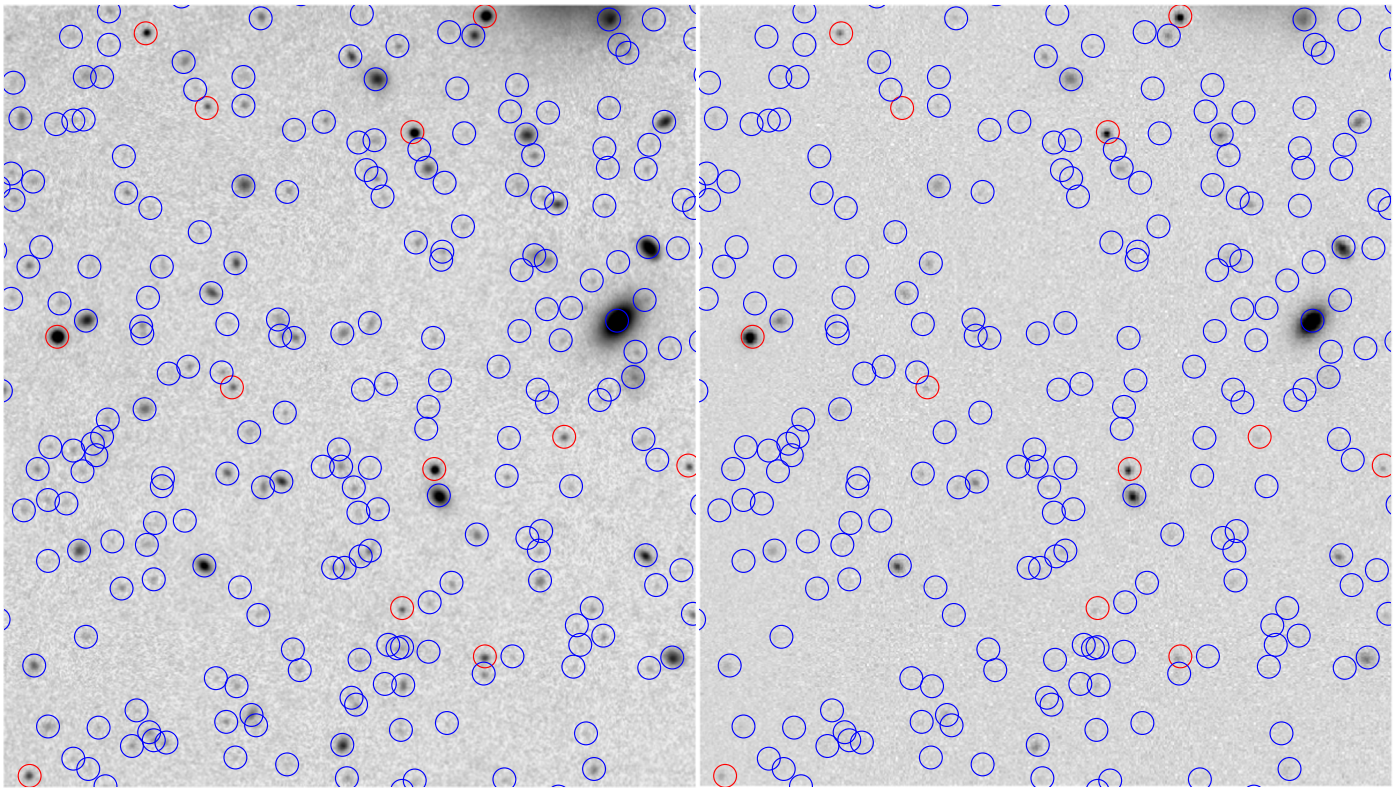

Figure 3. Illustration of the WVDECOMP-based detection in one of the cluster fields (circles). Blue circles are galaxies; red circles are stars identified by *SExtractor*. The left panel shows our *R*-band Magellan image. The right panel shows the *r*-band DES image of the same region, with Magellan detections superimposed.

stars are properly subtracted by our local background subtraction procedure.

3.3. Source Detection and Photometry

Our general strategy was to detect sources and measure galaxy fluxes in the *R* band and then measure fluxes at the same locations and within the same apertures in the *V* and *I* bands. Our procedure, detailed below, was designed to compensate for the difference in sensitivity and seeing in different filters and cluster locations and to ensure accurate photometry even for very faint galaxies.

3.3.1. Source Detection

We start with running a source detection algorithm on the combined *R*-band images. We used the wavelet decomposition algorithm, WVDECOMP, which is proven to be very efficient for detection of faint extended sources in X-ray images (Vikhlinin et al. 1998). We computed the noise map to properly set detection thresholds at each location. This is crucial for analyzing the faint galaxies in our Magellan images because pixel-to-pixel noise varies strongly within the field due to aliasing (see above) and nonuniform exposure coverage. The noise maps were empirically created from the data by convolving images cleaned from sources with the WVDECOMP's wavelet kernel and averaging the resulting rms deviations on 6″ spatial scales (see Appendix A for details). WVDECOMP uses this map for detection on the smallest scales; when proceeding to the largest scales, the noise map is appropriately smoothed further by the software (see Vikhlinin et al. 1998, for details).

The output from WVDECOMP is locations of statistically significant sources (Figure 3). We need a separate software package to apply additional selection criteria and measure galaxy fluxes. The first step is to identify and remove the likely stellar sources. To this end, we have run the *SExtractor* (Bertin & Arnouts 1996) detection on our *R*-band images, cross-matched the *SExtractor* and WVDECOMP source lists, and removed sources for which *SExtractor* measured stellarity indices >0.9. On average, $\approx 4\%$ of sources detected by WVDECOMP were removed by this procedure.

3.3.2. Fluxes and Colors

Our main goal with galaxy photometry is to reliably determine *total* luminosities for galaxies of different types and down to low fluxes. We also need to ensure that the flux measurements are consistent between exposures obtained in different filters and under different seeing conditions. Our approach is as follows. We assume that there are no color gradients within individual galaxies, as seems to be the case for outer regions of massive spheroidal galaxies (see, e.g., La Barbera et al. 2010; D'Souza et al. 2014). We fit the observed *R*-band (best-exposed filter) surface brightness profiles of each galaxy with an analytic model that includes the point-spread function (PSF) effects. This analytic fit is used to define the circular aperture size for subsequent flux measurement and determine the aperture correction. The apertures are chosen such that they are reasonably small to ensure good signal-to-noise in the flux measurements. At the same time, they are sufficiently large such that the differences in seeing between different nights and filters lead to negligible changes in the aperture correction factors.

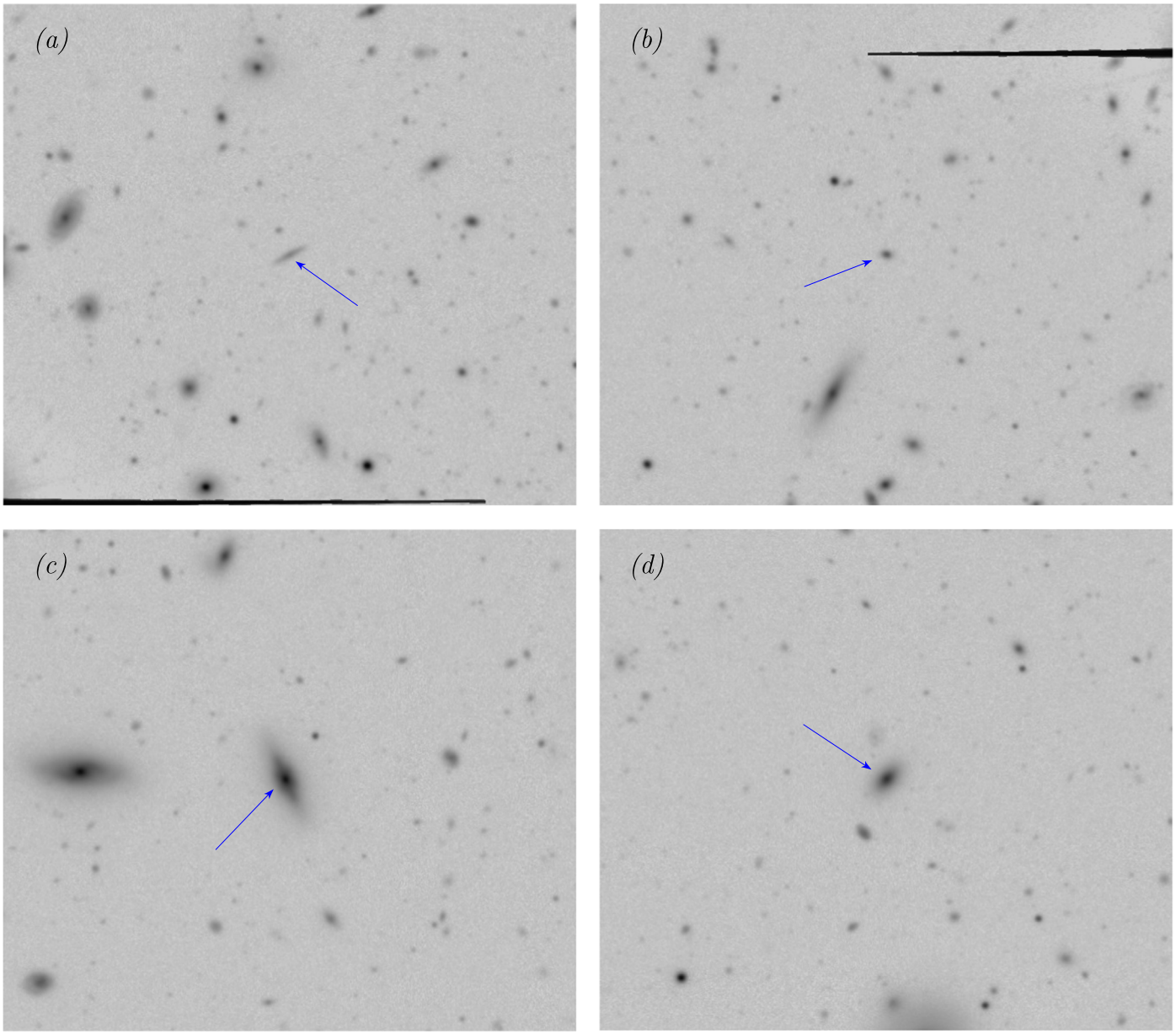

Figure 4. Examples of galaxies whose profiles and best-fit models are shown in Figure 5. Examples include bright and faint spirals and ellipticals.

The galaxy profiles were extracted in circular annuli, centered on the surface brightness peak determined by WVDECOMP. The annuli were of a constant log-width ($\lg(r_{\rm max}/r_{\rm min}) = 0.15$), with a maximum radius equal to 1.5 times the maximum distance from the source within this source's "island" (see Appendix A). The profiles exclude other sources detected in the vicinity by masking out the image pixels falling within these other sources' islands and scaling the measured flux in the partially masked annulus appropriately.

Our analytic model is motivated by the results of Kravtsov (2013), who showed that the stellar surface density profiles of galaxies of different morphological types have approximately similar shape at radii $r \gtrsim r_n$ and largely differ at $r \lesssim r_n$, where r_n is approximately a half-mass radius of stellar distribution. Within that radius, the profile of early-type galaxies is approximately described by the de Vaucouleurs model, while the late-type galaxies follow the exponential profile. We further note that Sérsic-type function, $I(r) \propto \exp(-7.669\,(r/r_0)^{\gamma})$, can describe both the de Vacouleurs model and the exponential model, depending on the values of r_0 and γ. The Kravtsov (2013) results indicate that the Sérsic index, γ, is not constant with radius but is changing near the radius r_n. We can approximate this by replacing r/r_0 with a function $z = y^{\alpha}(1+y^2)^{1-\alpha/2}$, where $y = r/r_0$. In this case, the effective Sérsic is γ for $r \gg r_0$, and $\gamma\,\alpha$ for $r \ll r_0$.

To account for the PSF effects, one ideally needs to convolve a 2D light distribution with a Gaussian and then convert the result back to the 1D radial profile. This approach is very computationally intensive. We found that instead of the 2D convolution, the PSF effects can be sufficiently accurately approximated by multiplying the profile by $\mathrm{erf}(r/p)$ where p is a free parameter fit individually for each galaxy. At $r \gg p$, this does not modify the profile, while at $r \ll p$, it introduces a flattening. Qualitatively, these are precisely the modifications expected from finite seeing.

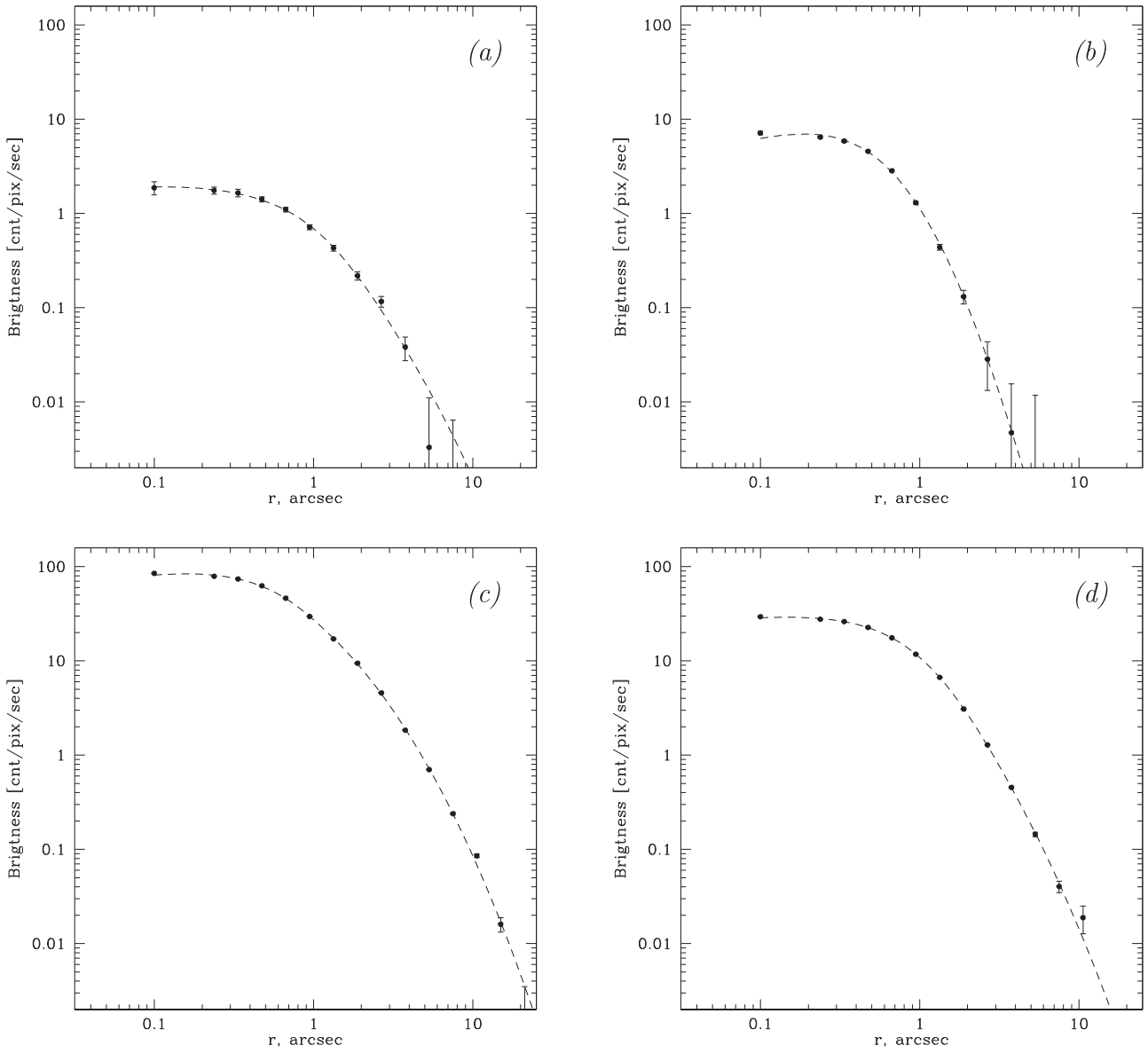

Figure 5. Surface brightness profiles and best-fit models (Equation (1)) for the galaxies shown in Figure 4. These examples include both spirals ((a) and (c)) and ellipticals ((b) and (d)).

To summarize, our analytic model is

$$I(r) = I_0 \exp(-7.669\, z^{\gamma}) \times \ \mathrm{erf}(r/p), \qquad (1)$$

where $z = y^{\alpha}(1 + y^2)^{1-\alpha/2}$, $y = r/r_0$, and I_0, r_0, α, γ, p are model parameters. We found that this model provides an accurate approximation to the data. The structural parameters (r_0, etc.) cannot be used literally because we treat the PSF effects approximately. However, the total galaxy luminosities can be obtained accurately, which is our goal. Examples of how this model fits the profiles of typical spiral and elliptical galaxies in our observations are shown in Figures 4–5.

To check that the method for flux measurement is accurate and stable, we performed the following test. The profile of Equation (1) with parameters fit to the *R*-band images for each galaxy was used to compute radii enclosing 50%, 70%, etc., of the total light. We then measured the *actual* flux within these radii and estimated total flux, as, e.g., $f_{\rm tot} = f_{50}/0.5$ and compared such estimate with the $f_{\rm tot}$ computed using the analytic profile. If our model provides an accurate description of the observed profiles, and the PSF effects are treated sufficiently accurately, the two estimates of $f_{\rm tot}$ should agree and such comparison thus represents a test of the accuracy of the model of Equation (1). In Figure 6, we show an excellent agreement of $f_{\rm tot}$ fluxes based on measurements in the r_{50} and r_{70} radii. Since all aperture definitions work equally well, we use the r_{50}-based fluxes in the following analysis, to maximize signal-to-noise.

To compute colors for each galaxy, we calculate the fluxes in the other filters using the apertures from the *R*-band, our deepest images. The same aperture corrections are applied to all filters. This is equivalent to an assumptions of no color gradients within individual galaxies; the central cluster galaxy is the only object where we accounted for the color gradients explicitly (see Section 5.2 below). However, we need to apply extra care in selecting the aperture size, because the seeing for data obtained in different filters can vary. We assume the PSF-related effects on the galaxy brightness profiles are small

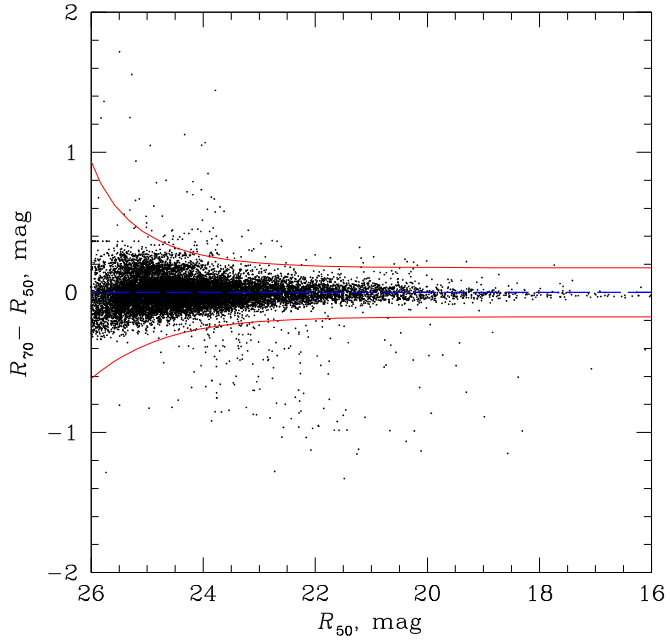

Figure 6. Comparison of the apparent R-band magnitudes of galaxies in the central cluster field, based on the aperture fluxes and correction factors for r_{50} and r_{70} radii (see the text). For the majority of objects, there is an excellent agreement of the two measurements, with a small scatter shown by the solid red lines. There is a small percentage of outliers outside of the main relations indicated by red lines to guide the eye. We have hand-checked a large number of those. The outliers with the positive deviations of the r_{70}-based magnitudes were all found to be spurious detections in the wings of bright stars and galaxies. They were eliminated from further analysis. The systematic offset between the two fluxes is only 0.03 mag.

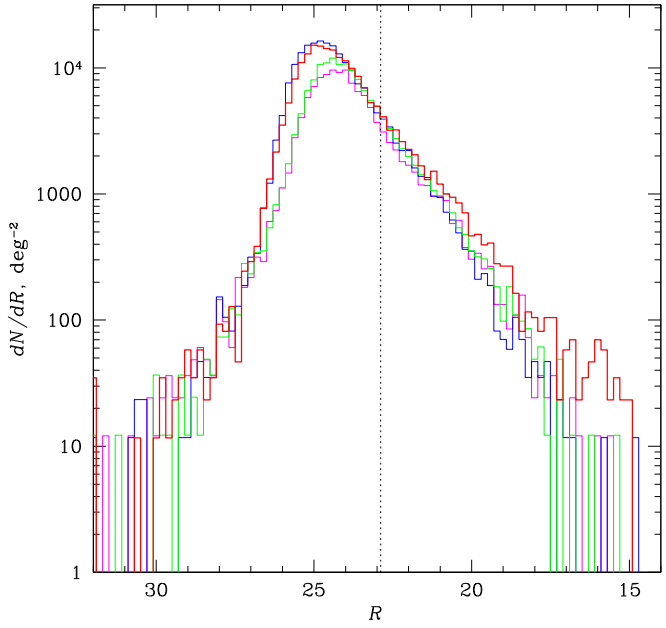

Figure 7. The differential $\log N - \log S$ distribution of detected galaxies in the central cluster field (red), and three background fields (blue, magenta, and green). The maximum in the $\log N - \log S$ histogram provides an estimate for a sensitivity limit in each field. The differences in the sensitivity limits primarily reflects differences in exposure. The vertical dotted line shows our adopted magnitude limit $R = 22.9$, which is conservative and applicable for all cluster and background fields.

outside the radius equal to the FWHM of the PSF in that observation. Therefore, the galaxy aperture was selected as the maximum of r_{50} and the PSF FWHM's for observations of the given field in R, V, and I filters. After the aperture size was determined this way, we computed the aperture flux corrections using the best-fit model in the R-band. In Figure 7 below, we show a comparison of galaxy number counts in different background fields, which shows an excellent agreement above their completeness limits despite the seeing varying from $0\farcs6$ to $1\farcs2$. This demonstrates that our modeling provides a sufficiently accurate treatment of the PSF effects. A similar excellent agreement in the source counts was found for the V- and I-band data.

The automated flux measurement procedure described above is very stable and works well for the vast majority of galaxies detected in the IMACS images. The only objects for which modifications were needed were bright, extended elliptical and spiral galaxies. For bright ellipticals, the main problem was that the locally measured background (Section 3.2) over-subtracted the outer wings of the galaxy profiles. Since for bright objects, small residuals variations are not an issue, we simply reapplied our modeling algorithm to the global background-subtracted images. For bright spirals, the main issue was that the WVDECOMP algorithm splits the galaxy into many individual objects, corresponding to the surface brightness clumps in the spiral arms. We visually identified such cases and re-measured fluxes in elliptical apertures using global background-subtracted images (see an example shown in Figure 8). Such cases are easily identifiable by visual inspection of Magellan images with overlaid WVDECOMP detections. Typically, there are ~10 such objects in one image, or <5% of the total number of galaxies ultimately used for determination of the cluster stellar mass.

3.3.3. Completeness Limits

The difference in total accumulated exposure in different locations leads to the differences in the completeness limit. To simplify the joint analysis of the entire A133 data set, we need to define a single completeness limit. We identify completeness for each field, using the peak location in the differential $\log N - \log S$ distributions. Examples are shown in Figure 7. The red histogram shows the source counts in the central cluster field, and the other three histograms show example source counts in the background fields. The maxima in the $\log N - \log S$ distributions are well defined, but broad, possibly because of substantial flux measurement uncertainties near the threshold sensitivity. To avoid this problem, we set a threshold for further analysis at ≈1 mag brighter than the maximal point in the $\log N - \log S$ curves at $m \sim 24$. The adopted magnitude limits are $R = 22.9$ and $V = 22.6$. In the R-band, this limit corresponds to an absolute magnitude of $M_R = -14.1$ at the cluster distance. This is ≈5.4 magnitudes below M^* of the R-band field galaxy luminosity function (Lin et al. 1996).

3.4. Red Sequence

Spectroscopic redshifts are unavailable for the majority of galaxies detected in the IMACS fields (Connor et al. 2018). Therefore, we need to subtract the statistical background, which corresponds to the contribution of foreground and background galaxies to the galaxy stellar-mass functions, cluster light profile, etc. These contributions were measured in our offset background fields (see Section 3 above). The

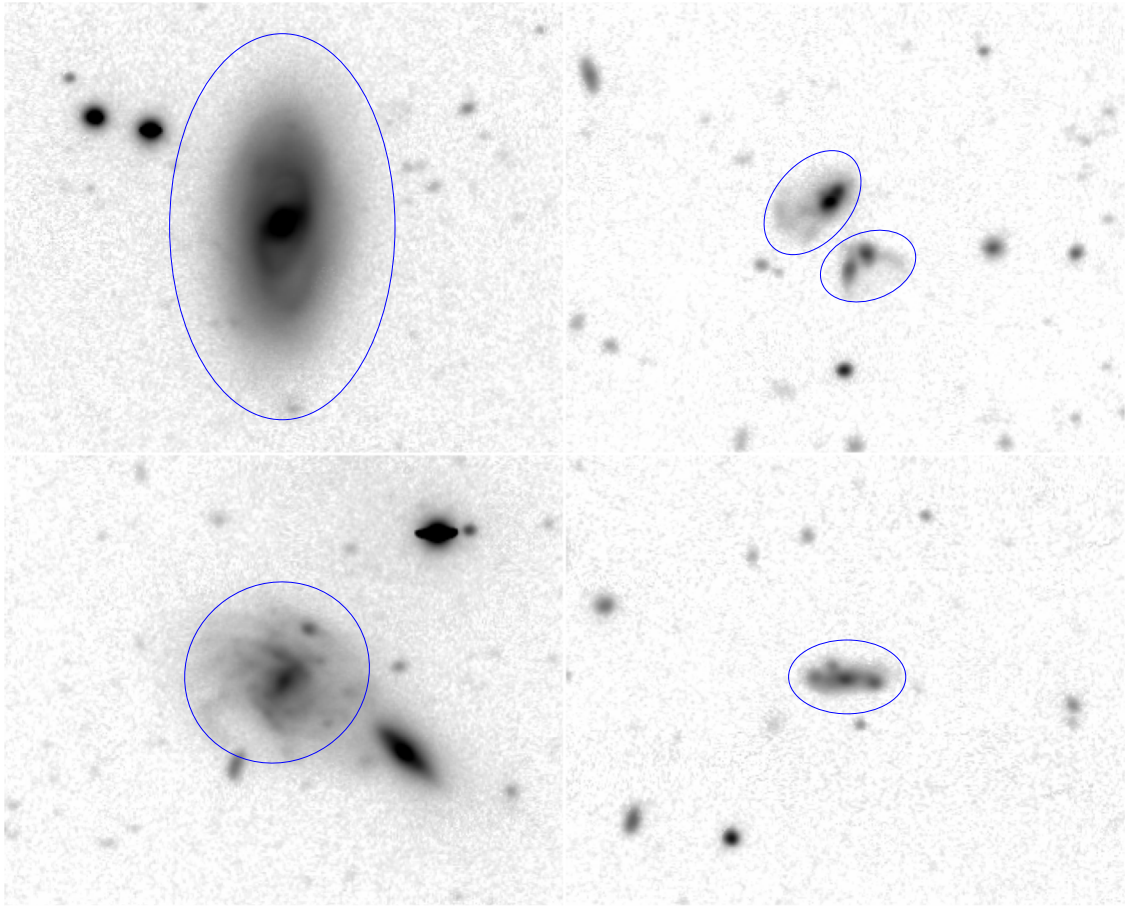

Figure 8. Examples of elliptical apertures used for flux measurements in bright spiral galaxies with complex morphology. Our source detection algorithm fails for such galaxies because it splits them into several objects. Therefore, their fluxes were re-measured in hand-set elliptical apertures.

surface number density contrast of the cluster members relative to the statistical background of galaxies with the same apparent magnitude is low, except for the central pointing (e.g., Figure 7). Therefore, we conservatively use additional selection criteria to remove galaxies unlikely to be associated with A133.

Our selection is based on the cluster red-sequence method extensively used for studies and identification of galaxy clusters (e.g., Bower et al. 1992a, 1992b; Gladders et al. 1998; López-Cruz et al. 2004; Koester et al. 2007; Valentinuzzi et al. 2011; Rykoff et al. 2014). The underlying idea is that red, passively evolving cluster members have similar colors and form a narrow sequence in the color–magnitude diagram. Some of the galaxies within the cluster, e.g., those with recent bursts of star formation, can be bluer than the red sequence (e.g., Connor et al. 2019a). However, there should be very few, if any, galaxies redder than the red sequence members because those members have the oldest stellar populations. The small number of objects above the red sequence are "special cases," such as dust-covered AGNs, in which the stellar-mass measurements based on optical luminosities are problematic. Empirically, these considerations are confirmed by the colors of the A133 members with spectroscopic redshifts (Figure 9).

For the A133 analysis, we used the $V - R$ color–magnitude diagram. This diagram for the central field (Figure 9) clearly shows the red sequence corresponding to the A133 redshift. We selected potential cluster members as the objects below or just above the cluster red sequence, $V - R < 1.13 - 0.025R$, and brighter than the completeness limits for the R- and V-band images (recall that these are $R = 22.9$ and $V = 22.6$, see Section 3.3.3). These criteria select a pink-shaded region in the color–magnitude diagram.

We emphasize again that these selection criteria are conservative. To improve the cluster contrast still further, we could have used a narrow color band around the red sequence, or additional selection criteria such as galaxy apparent sizes. However, we then would risk missing some of the cluster members with unusual properties. Since our main goal is the maximally complete census of the cluster stars, we use more inclusive selection criteria described above.

In addition to A133's red sequence, the color–magnitude diagram seems to show a second sequence with redder colors, $V - R \approx 0.95$ at $R \approx 20$. We attribute it to the background cluster projected onto the core A133, for the following reasons. There is indeed a group of redder galaxies with smaller diameter in this region (Figure 2). The brightest of these redder galaxies, at R.A. = 01:02:45.2 and decl. = −21:54:14, has a measured spectroscopic redshift, $z = 0.293$. The location of that second red sequence is in excellent agreement with the red sequence of Z3146 ($z = 0.2906$) measured by Kausch et al. (2007) in the same filters. Most of galaxies in this background cluster should be excluded by our color–magnitude selection of potential A133 members.

Selection of potential cluster members by means of the color–magnitude diagram concludes our preliminary data

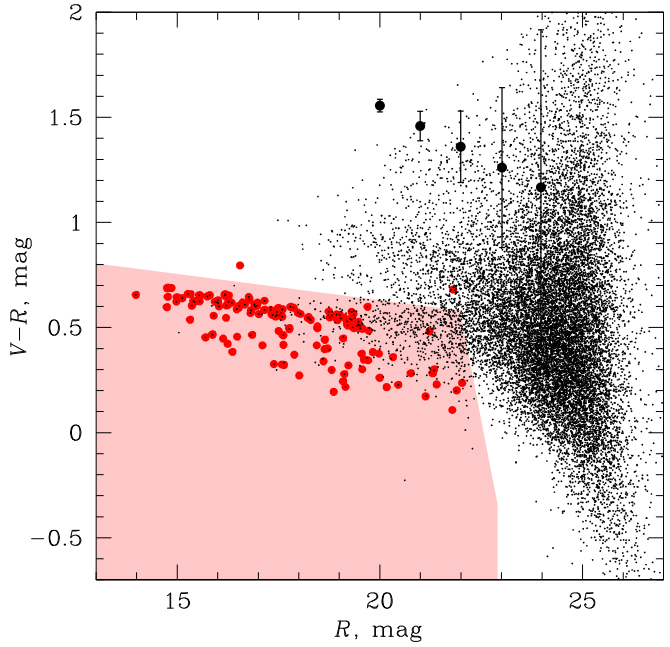

Figure 9. Color–magnitude diagram for galaxies in the central cluster field. The shaded region shows our selection criteria for A133 members. This region is limited by the R and V magnitude limits on the right and by the color–magnitude cut on the top. Red points represent cluster galaxies with known spectroscopic redshifts over all cluster fields (Connor et al. 2018). The points with vertical errorbars indicate typical uncertainties of the $V-R$ color.

analysis steps. In what follows, we describe how stellar masses of individual galaxies were estimated from the optical luminosities and how they were used to derive the stellar-mass functions and the total stellar-mass profiles within the cluster.

4. Results: Stellar-mass Function of the Cluster Members

4.1. Galaxy Stellar-mass Estimates

Using the measured R-band magnitudes and $V-R$ colors, we estimated the stellar mass of each galaxy. The method is based on the stellar populations synthesis models from Bell et al. (2003). The first step is to convert the apparent magnitudes to the absolute magnitudes in R- and V-bands. We used the standard relation, $M = m - 25 - \log(D_L\ \mathrm{Mpc}) - A - K(z) - \mathrm{EC}$, where D_L is the luminosity distance, A is the interstellar extinction correction from Schlegel et al. (1998), $K(z)$ is the K-correction, and EC is the evolutionary correction. The K-corrections were obtained from the "K-correction calculator" (Chilingarian et al. 2010; Chilingarian & Zolotukhin 2012).[10] The evolutionary correction EC is adopted from Poggianti (1997) where it is provided for different galaxy types and a set of photometric bands. We used the EC values averaged over galaxy types. We also note that the evolutionary correction, $\mathrm{EC} = -0.08$, is small at the A133 redshift in both our filters. The described procedure is used to estimate $z = 0$ absolute magnitude in the R band and a de-redshifted $M_V - M_R$ color for each galaxy.

To obtain the stellar mass from these parameters, we convert the R-band absolute magnitude to the luminosity in solar units using $M_{R,\odot} = 4.42$ for the absolute R-band magnitude of the Sun (Binney & Merrifield 1998). The luminosity is then converted to the stellar mass. This conversion is a function of the $M_V - M_R$ color. Using the Bell et al. (2003) fitting formulae for $M_\star/L_R$ as a function of $M_B - M_V$ and $M_B - M_R$, we obtain (in solar units):

$$\lg(M_\star/L_R) = -0.528 + 1.818(M_V - M_R). \quad (2)$$

The main uncertainty in the derived stellar masses is due to assumptions on the initial mass function of the stellar population that enter the population synthesis models. Note that the Bell et al. calibration used the "diet Salpeter" IMF model (see discussion in Section 2.4 of Kravtsov et al. 2018 regarding this choice of the IMF model and its effects on the stellar-mass determination). In this work, we will use the "diet Salpeter" based masses. To convert to, e.g., the Chabrier (2003) IMF, our stellar masses should be scaled down by 0.1 dex.

4.2. Stellar-mass Functions of A133 Galaxies

Before deriving the total cluster stellar mass as a function of radius, we need to explore how much light or stellar mass we may be missing below the completeness limits of our data. We address this question by analyzing the stellar-mass functions of A133 galaxies.

In Figure 10, we show the mass functions measured in the central and off-center cluster fields, normalized to the unit area on the sky. The background number density of galaxies has been measured using our off-cluster pointings and subtracted from these data. The observed mass functions show a roll-over below $M_\star \approx 2 \times 10^8 M_\odot$. To avoid incompleteness in our stellar-mass measurements, we use only galaxies with $M_\star > 3 \times 10^8\, M_\odot$ in the following analysis. To account for the stellar mass potentially "lost" below this threshold, we estimate fractional correction factors using analytic fits to the mass function (see below).

Another prominent signature apparent from Figure 10 is a two-component structure of the mass function in the central pointing (filled circles in the figure). Above $\approx 4 \times 10^9\, M_\odot$, it follows a Schechter-type (Schechter 1976) function with an exponential cutoff around $M_\star \approx 10^{11}\, M_\odot$. At lower masses, the stellar-mass function steepens and its behavior is consistent with a power law down to our completeness limit. However, the mass function cannot be adequately fit with a single Schechter model over a broad mass range. The two-component form of the mass function in the central field is supported by comparison with the mass function in the off-center fields (open circles in Figure 10). This later mass function is consistent with a power law with the same slope as that for the faint end of the mass function near the cluster center. The existence of two separate components is also supported by the radial profile analysis in different mass ranges (see Section 5.1 below). Following all of these considerations, we modeled the central mass function separately above and below the "ankle" at $M_\star = 4 \times 10^9\, M_\odot$. Above this mass, we use a Schechter model:

$$\frac{dN}{d\lg M} = N_0 \left(\frac{M}{M_0}\right)^\alpha \exp\left(-\frac{M}{M_0}\right), \quad (3)$$

where N_0, M_0, α are fitted parameters. In practice, α is unconstrained, given a small dynamical range in masses for the bright end of the mass function. Therefore, we fixed $\alpha = 0$.

For the mass function in the off-center fields, we used a pure power-law model (dashed line in Figure 10). The best-fit power-law slope is $\alpha = -0.55 \pm 0.11$. The analytic model of the central mass function in the $3 \times 10^8\, M_\odot < M_\star < 4 \times 10^9\, M_\odot$ range is

[10] Available on http://kcor.sai.msu.ru.

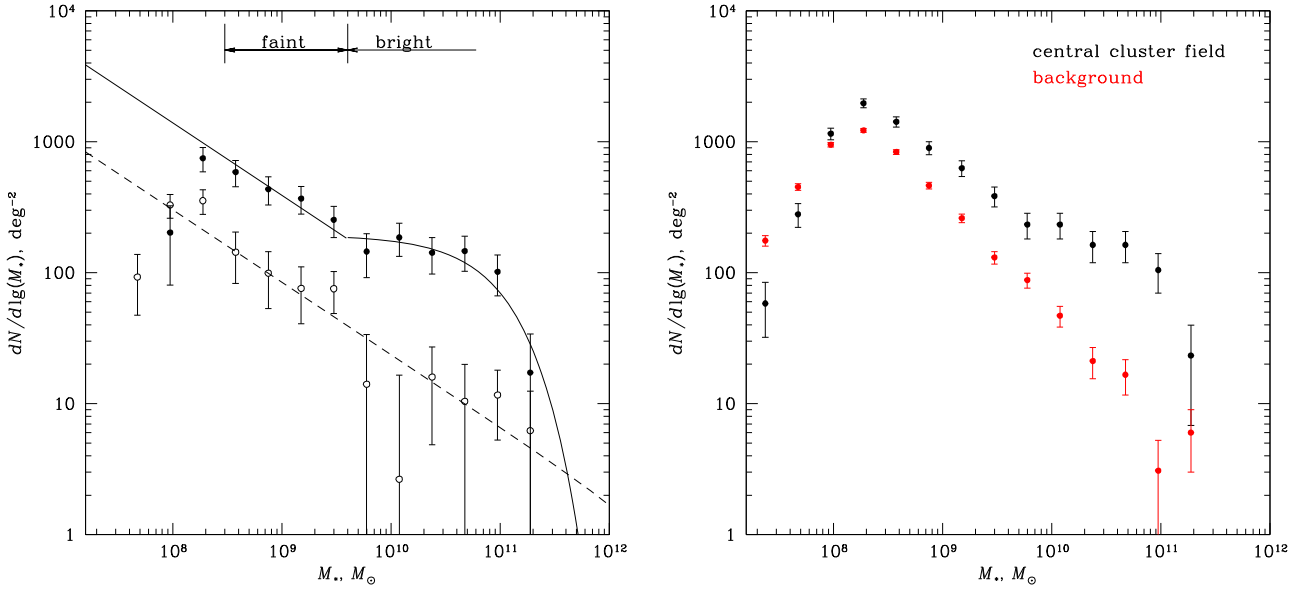

Figure 10. Stellar-mass function for galaxies in the central and off-center cluster fields (filled and open circles, respectively), normalized to the area on the sky. The cluster BCG is excluded from this plot. The solid and dashed lines show the best-fit power-law+exponential and power-law models (see Equation (3) and accompanying text). The right panel shows the raw data for the central field and the background, to illustrate that detection of the two-component structure of the stellar-mass function is indeed robust. The data for the left panel of this figure is available at an online repository doi:10.5281/zenodo.3610482.

obtained by using a power law with the same fixed slope $\alpha_0 = -0.55$ and a normalization chosen to match the Schechter fit (Equation (3)) for brighter galaxies at $M_\star = 4 \times 10^9\,M_\odot$. This fit is also shown by the solid line in Figure 10. It provides a good description to the data.

We note that the total mass for a power-law mass function with a slope of $\alpha = -0.55$ converges at the faint end. Therefore, there is no evidence that we may be missing a significant population of dwarf galaxies, which is important for the total stellar-mass budget in the cluster. We also note that if there were a significant population of undetectable galaxies, especially in the cluster center, it would contribute to the extended diffuse light envelope, which we analyze and account for separately (Section 5.2). In the following analysis, we assume that the power-law behavior continues to extremely low masses, and we apply the corresponding "incompleteness" correction of $\times 1.45$ for the total mass of galaxies with $M_\star < 4 \times 10^9\,M_\odot$. The galaxies with $M_\star > 4 \times 10^9\,M_\odot$ are counted and modeled separately (see below), and they require no incompleteness corrections.

5. Results: Stellar-mass Profile

Using the results for the stellar-mass function of the cluster members, we proceed to a derivation of the stellar-mass profile in the cluster. Our general approach is to directly count the contribution of each galaxy with estimated mass $M_\star > 3 \times 10^8\,M_\odot$ and then correct the total for incompleteness at the faint end of the mass function (see above). We derived the stellar-mass profile of the brightest cluster galaxy separately, tracing the wings of its light profile to $R \approx 200$ kpc. The derived projected profiles of both the BCG and other cluster galaxies are fit to analytic functions defined in 3D, and so deprojection is straightforward.

5.1. Contribution from Cluster Member Galaxies

To determine the stellar-mass profile for non-central galaxies, we computed the surface mass density in radial bins of equal log-width, centered on the BCG. Since there are indications that the mass function of the cluster members has two distinct components, we computed the surface mass density separately in two mass intervals, $3 \times 10^8 < M_\star < 4 \times 10^9\,M_\odot$ and $M_\star > 4 \times 10^9\,M_\odot$. The lower boundary corresponds to the estimated completeness limit, and the middle point corresponds to the "ankle" in the mass function (Figure 10). In the same mass ranges, we computed the contribution of background galaxies to the surface mass density, using the data from eight background fields. This statistical background was subtracted from the projected cluster mass profiles.

The results are shown in Figure 11. Indeed, the figure shows different radial profiles for the massive and lower-mass galaxies, which reflects a well known radial dependence of the dwarf-to-giant galaxy fraction in clusters (e.g., Smith et al. 1997; Barkhouse et al. 2009). The lower-mass galaxies have a power-law type profile with a projected slope of -0.77 ± 0.20. The profile for massive galaxies has a flat core out to $R \approx 400$–500 kpc (nearly $0.5\,r_{500c}$). Beyond this radius, the profile steepens. While the measured profiles are quite noisy, there is still a tentative detection of the cluster signal in both components out to at least $\approx$2 Mpc, beyond the estimated r_{200c} radius.

To deproject these profiles, we fit them using a projected analytic function defined in 3D. Specifically, we used a "Nuker" density profile (see Lauer et al. 1995; Kravtsov et al. 1998), which can be viewed as a generalized version of the Navarro–Frenk–White (NFW; Navarro et al. 1997) profile:

$$\rho(x) = \frac{\rho_0}{x^\alpha (1 + x^\gamma)^{(\beta-\alpha)/\gamma}}, \qquad (4)$$

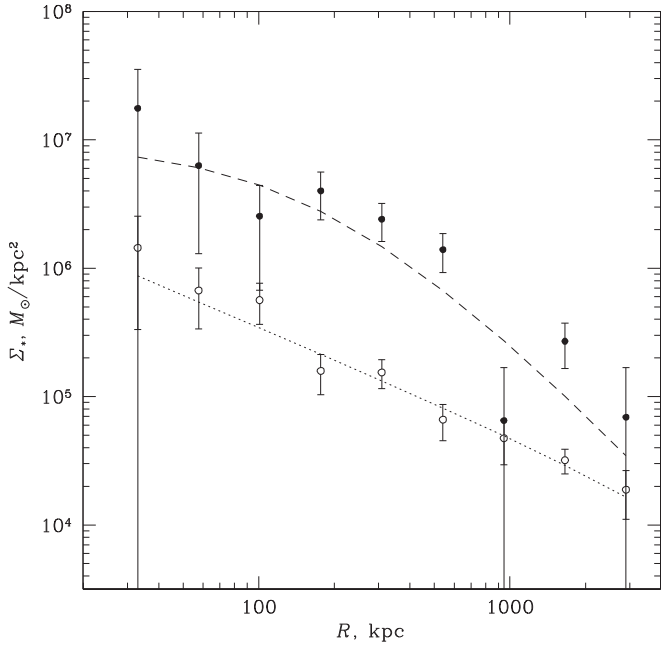

Figure 11. The projected cluster stellar-mass profile, derived for galaxies with individual masses in the ranges (3–40) $\times 10^8\,M_\odot$ (open circles) and (40–2500) $\times 10^8\,M_\odot$ (filled circles). The lines show the best-fit model (see Equation (4) and accompanying text). The difference in shape in the two mass profiles is insensitive to the exact choice of the boundary between "faint" and "bright" galaxies.

where $x = r/r_s$, r_s is the scale radius, and ρ_0 is the density scale. The profile inner slope is controlled by α, β controls the outer slope, and γ determines how fast the profile slope changes around $r = r_s$. This model has been numerically integrated along the line of sight and fit to the data.

Since our measured profiles are noisy, we did not fit all parameters independently. For massive galaxies, we fitted ρ_0 and r_s and fixed the inner slope at $\alpha = 0$, the outer slope at $\beta = 3$ as expected in the NFW models, and also fixed $\gamma = 1$. For the low-mass galaxies, we used a power-law limit of Equation (4) by fixing r_s at a high value. The best-fit projected profiles are shown as dashed lines in Figure 11.

The 3D radial profile of the stellar mass in the cluster can be obtained straightforwardly by integrating the best-fit density profile of Equation (4). To estimate the statistical uncertainties of the derived mass profiles, we used the Monte-Carlo method described in Vikhlinin et al. (2006). We generated multiple realizations of the data by scattering the profile data points according to their statistical uncertainties, re-fit the models, re-derived the mass profiles, and computed the scatter of mass values at each radius, averaged over the realizations. The resulting stellar-mass profiles with uncertainties are shown in Figure 15 below.

5.2. Brightest Cluster Galaxy

The contribution of the brightest cluster galaxy to the stellar-mass budget was considered separately because this galaxy is bright and very extended and, therefore, cannot be treated as a point mass. We start by extracting the BCG light profiles in the R, V, and I filters. Unlike the analysis of non-central galaxies, we used the global background subtraction (Section 3.2) because the locally estimated background subtracts the extended wings of the BCG profile. Unfortunately, the global background subtraction is less accurate, leading to increased uncertainties of the BCG profile at large radii. To estimate the level of these uncertainties, we extracted R, V, and I-band light profiles around three representative locations in each of the background and cluster off-center pointings not contaminated by bright stars.

The resulting light profile of the BCG in R, V, and I filters is shown in Figure 12. We have applied uniform offsets -0.66 and $+0.64$ mag per arcsec^2 to the V and I-band profiles, respectively, to match the R-band brightness at small radii. Note that this BCG $V - R$ color exactly corresponds to the red sequence location for the brightest cluster members (Figure 9). The level of estimated background subtraction uncertainties in the R-band is shown by a hatched region. The observed light profiles in all three filters follow one another very precisely out to $r \approx 150$ kpc where the R-band brightness reaches a 26 mag arcsec^{-2} level. Outside this radius, the V- and I-band profiles continue to follow one another, while the R-band brightness shows a significant positive deviation. A brightness excess appearing only in the R band is not expected for normal stellar population spectra, where systematic trends run from V through R to I. Therefore, a more likely cause of the observed R-band excess is inaccuracies in the global background subtraction at these low surface brightness limits. We find that an additional, uniform, background correction of 26.9 mag arcsec^{-2} in the R-band is sufficient to completely match the data in all three filters (Figure 13). This is only 60% higher than the typical observed level of background variations at $R = 200$ kpc, and so such corrections are very likely. We use the R-band profile with this additional background correction in the analysis below. However, we recognize that the measurements become extremely sensitive to the background subtraction at $R > 200$ kpc, and therefore, we restrict the mass measurements to within this radius.[11] In Figure 14, we show a zoom-in on the composite R-band image near the BCG location. The 200 kpc radius is shown by the red circle. The wings of the BCG brightness in the NE and SW directions can indeed be traced visually very close to this radius.

To reconstruct the 3D stellar-mass profile of the BCG, we use an approach similar to that in Section 5.1. We fit the observed light profile with a projected density model defined in 3D and then integrate that model as a function of radius. In this case, we used a modified β-model (see Vikhlinin et al. 2006):

$$\rho(r) = \frac{\rho_0}{(1 + (r/r_c)^2)^{3\beta}} \frac{1}{(1 + (r/r_s)^\gamma)^{\epsilon/\gamma}}, \qquad (5)$$

where ρ_0, r_c, r_s, β, γ, ϵ are fitted parameters. This model describes a flattening at small radii ($r \lesssim r_c$), a transition to a power-law behavior at $r > r_c$, and a further change of the profile slope at large radii, $r \gtrsim r_s$. The best-fit model is shown by the solid black line in Figure 13 and provides an excellent fit to the data. Its best-fit parameters are $\rho_0 = 24.1$ mag arcsec^{-2} kpc^{-1}, $r_c = 2.5$ kpc, $r_s = 245.1$ kpc, $\beta = 0.42$, $\gamma = 2.3$, $\epsilon = 0.76$. We use this model to compute the R-band luminosity of the BCG as a function of 3D radius.

[11] If one assumes that the R-band profile should not be corrected and integrates it to 400 kpc, this leads to a 33% increase in the estimated BCG stellar mass, or an 11% increase in the stellar mass of A133 within the r_{500c} radius.

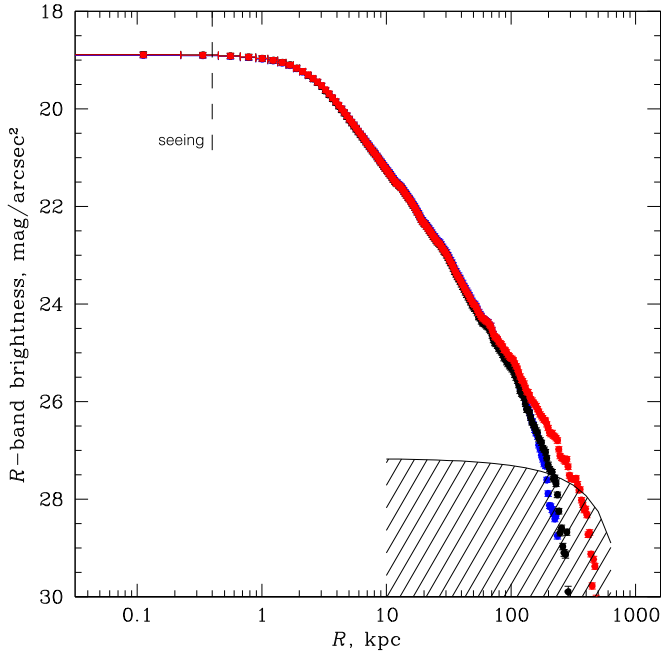

Figure 12. The raw BCG light profile in three filters R (red), V (blue), and I (black). For clarity, the V- and I-band profiles were renormalized to match the R-band profile at small radii. The shaded region shows a level of estimated background uncertainties as a function of radius (see the text).

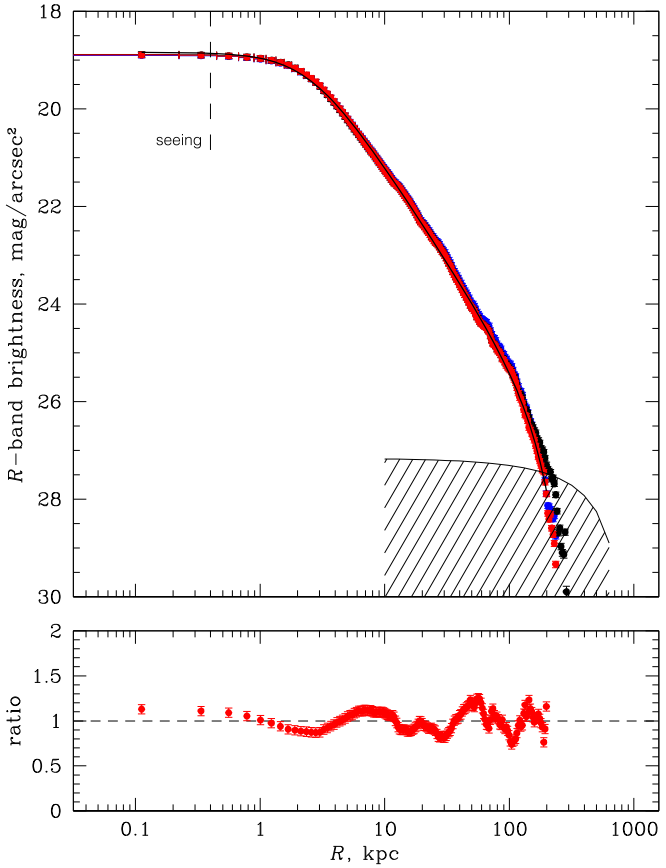

Figure 13. Same as Figure 12, but with the uniform background correction applied to the R-band data (see the text). The black solid line shows the best-fit model (see Equation (5) and accompanying text). The bottom panel shows model residuals.

To convert this luminosity to the stellar mass, we use the mass-to-light ratio from Bell et al. (2003), just like we did for the other cluster members. There is only a small change in the observed color with radius: $V-R=0.66$ at the BCG center, dropping to $V-R=0.56$ at $r=50$ kpc, beyond which the contribution of systematic background uncertainties (see above) makes color gradient measurements unreliable. Note that such color gradients are quite common in the BCG and the intracluster light (DeMaio et al. 2018). The corresponding change in the M/L ratio, from $3.9\,M_{\odot}/L_{\odot}$ in the center to $2.6\,M_{\odot}/L_{\odot}$ at 50 kpc, was included in the conversion of the observed light profile to stellar mass. If, instead, one uses a fixed $V-R$ color measured at the center, the BCG stellar mass within 200 kpc is overestimated by 59%.

Finally, we note that the formal statistical uncertainties of the BCG light profile within 200 kpc are very small. The mass uncertainties should be completely dominated by those in the M/L ratio (e.g., those related to the color gradient or assumptions on the IMF in the the stellar population synthesis models, see Section 4.1).

5.3. Total Stellar-mass Profile

In Figure 15, we show the total reconstructed stellar-mass profile within A133 and its individual components discussed above (estimates of $M_{\star}$ within different r are also presented in Table 1). For comparison, we also show the profile of the hot gas and of the total mass reconstructed from the X-ray data (A. Vikhlinin et al. 2020, in preparation, see also, Vikhlinin et al. 2006). Several points about these profiles are noteworthy.

The central cluster galaxy contributes a large fraction of the total stellar mass. Its integrated mass within 200 kpc is approximately 50% of the rest of cluster galaxies within 1 Mpc ($\approx r_{500c}$), or ~25% at $r\approx 3$ Mpc (well outside of r_{200c}). The BCG dominates the total baryon mass, including hot gas, in the central ≈100 kpc. The hot gas within this radius shows a spike in metallicity (see Figure 3 in Vikhlinin et al. 2005), likely reflecting extra enrichment due to stellar mass loss and supernovae within the BCG.

Non-central galaxies approximately follow the distribution of total mass in the radial range $\approx(0.1\text{–}1)\,r_{500c}$ where both the X-ray and optical measurements are most reliable. This is in line with a number of earlier studies for different clusters (e.g., Andreon 2015; Palmese et al. 2016).

Small-mass galaxies of $M_{\star}<4\times10^{9}\,M_{\odot}$ contribute a minor fraction of the total stellar mass even at large radii. At $r=3$ Mpc, their contribution is ≈13%, and it is even lower at smaller radii. The majority of the cluster stellar mass is contributed by bright galaxies and the BCG. Nevertheless, the radial distribution of these faint galaxies is quite distinct from the radial distribution of brighter galaxies (see Section 5.1 above). Namely, the radial distribution of stellar mass of faint galaxies is well described by a single power-law profile, $\rho(r)\propto r^{-1.77\pm0.20}$. We discuss possible interpretations of this fact in Section 6 below.

Finally, we note that at $r=r_{500c}$ and beyond, the stellar mass is a small fraction of the total baryonic mass (i.e., gas + stars), ≈11%. This is consistent with the values previously reported in the literature (e.g., Gonzalez et al. 2013; Kravtsov et al. 2018). Therefore, despite using much deeper data and an ability to trace the BCG light profile to larger radii, we have not uncovered a major reservoir of cluster baryons associated with

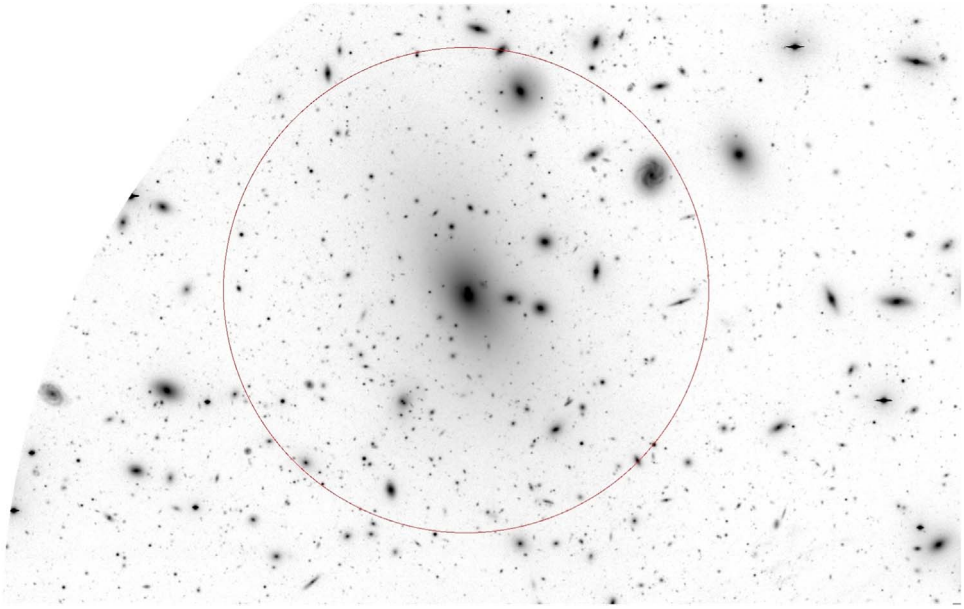

Figure 14. Central cluster region around the BCG galaxy in the *R*-band. The red circle shows a region of 200 kpc radius where we measured the BCG light profile. The wings of the BCG brightness in the NE and SW directions can indeed be traced visually very close to this radius.

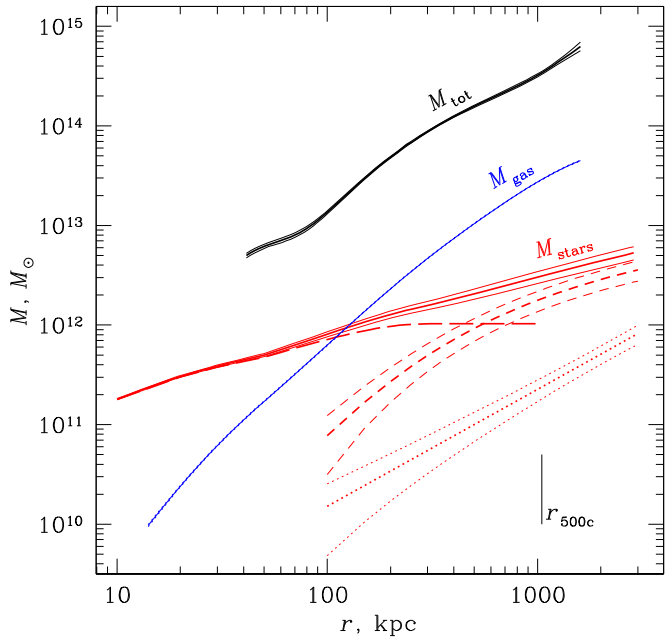

Figure 15. 3D profile of enclosed stellar mass of the three stellar components: the red dotted line is for low-mass cluster galaxies of $M_\star = (3\text{–}40) \times 10^8\,M_\odot$, the red dashed line shows high-mass cluster galaxies of $M_\star = (40\text{–}2500) \times 10^8\,M_\odot$, and the red long dashed line represents the BCG. The solid red line shows the summed profile of the three stellar components of the cluster. Blue is the X-ray estimated mass profile of gas and black line is the total mass profile derived from *Chandra* X-ray data using hydrostatic equilibrium assumption (A. Vikhlinin et al. 2020, in preparation). Short vertical black line indicates the r_{500c} radius.

cluster galaxies. To substantially increase the fraction of stellar mass in the cluster baryon budget requires drastic revisions of the M/L ratio values from stellar population synthesis. Such revisions are not supported by detailed modeling of the galaxy spectra (van Dokkum et al. 2017). We will present a detailed analysis of the matter components in A133, including dark matter and hot intracluster gas, in a subsequent paper.

Table 1
Stellar-mass Measurements in A133

r/r_{500c}	r, kpc	$M_{\rm BCG}$	$M_{\rm bright}$	$M_{\rm faint}$	$M_{\rm stars}$
0.1	105	7.4	0.87 ± 0.49	0.16 ± 0.11	8.4 ± 0.5
0.2	262	10.2	4.1 ± 1.4	0.47 ± 0.21	14.8 ± 1.4
0.5	524	10.3	9.7 ± 2.5	1.06 ± 0.34	21.1 ± 2.5
1.0	1048	10.3	18.4 ± 4.2	2.4 ± 0.6	31.1 ± 4.2
1.5	1572	10.3	24.6 ± 5.5	3.8 ± 0.8	38.7 ± 5.6
2.5	2620	10.3	33.4 ± 7.6	7.0 ± 1.5	50.7 ± 7.8

Note. All masses are in units of $10^{11}\,M_\odot$ and computed for our default cosmology. The last column gives the total of the three components—the BCG, bright galaxies, and faint galaxies.

6. Discussion of the Radial Dependence of Galaxy Stellar-mass Function

One of the key results of this paper is the upturn of the stellar-mass function of satellite galaxies in A133 at $M_\star \lesssim 4 \times 10^8\,M_\odot$. The best-fit slope α of the power law in this dwarf galaxy regime is comparable with recent measurements of the faint-end slope of the stellar-mass function of field galaxies of -0.5 ± 0.05 at $z = 0.1$ (see, e.g., Wright et al. 2017, and references therein) and at higher redshifts (Papovich et al. 2018; Wright et al. 2018).

The existence of the upturn in the luminosity function in clusters and the value of the faint-end slope have long been a subject of debate in the literature (e.g., Driver et al. 1994; Smith et al. 1997; Barkhouse et al. 2007; Rines & Geller 2008; Harsono & De Propris 2009; Agulli et al. 2014), which may be due to real diversity of the luminosity functions in clusters (e.g., Moretti et al. 2015) and, partly, due to degeneracy among model parameters in double-Schechter fits to LF. Nevertheless, the overall shape of the stellar-mass function and its slope in the dwarf galaxy regime are qualitatively consistent with the form of *R*-band luminosity function measured in several nearby clusters (Smith et al. 1997) and groups (Zabludoff & Mulchaey 2000). In

addition, recent systematic study of luminosity function of galaxies in the SDSS groups and clusters by Lan et al. (2016) reported a Schechter+power-law shape qualitatively similar to that we measured for A133.

Another intriguing result of this study is that the shape of the stellar-mass function changes with radius. This is reflected in the difference in the radial distribution of low- and high-luminosity galaxies (Figure 11). It is likely that this difference is related to the decrease of the "dwarf-to-giant ratio" toward cluster center that was previously reported in several clusters (e.g., Smith et al. 1997; Sánchez-Janssen et al. 2008; Barkhouse et al. 2009).

Cosmological simulations of structure formation in the ΛCDM model predict that mass and radial distributions of host halos of satellite galaxies are nearly self-similar (e.g., Kravtsov et al. 2004; Nagai & Kravtsov 2005; Hellwing et al. 2016; van den Bosch & Jiang 2016) throughout most of the cluster volume. The recent study by Han et al. (2018) indicates that this self-similarity is broken at $r/R_{200} \lesssim 0.2$, where massive halos have steeper radial distribution resulting in a smaller dwarf-to-giant halo ratio at these radii. The difference is due to dynamical friction experienced by massive halos, which brings them closer to the cluster center.

However, the difference in the radial distribution of dwarf and luminous galaxies in A133 persists out to $r \sim R_{200}$ and, thus, is unlikely to be due solely to dynamical friction. The significant difference in radial and stellar-mass distribution of galaxies of different mass is likely to be yet another manifestation of the break of self-similarity of galaxy properties due to star formation and feedback processes accompanying galaxy formation (see Somerville & Davé 2015; Naab & Ostriker 2017, for reviews).

One of the potential consequences of feedback in dwarf galaxies is flattening of their central dark-matter density profiles (Navarro et al. 1996; Mashchenko et al. 2008; Pontzen & Governato 2012)—the effect that is most efficient for galaxies of stellar mass $M_\star \sim 10^9$–$10^{10}\,M_\odot$ (e.g., see Section 3.1.1 in Bullock & Boylan-Kolchin 2017, for a review). Another effect of galaxy formation that breaks self-similarity is that gas mass fractions are, on average, much larger in dwarf galaxies compared to the giant galaxies. Gas-rich dwarfs suffer both tidal stripping and ram pressure stripping of halo and interstellar gas. The latter, if sufficiently fast, can lead to a rapid decrease of the gravitational potential depth in the inner regions and significant enhancement of tidal stripping of the stellar component in dwarf galaxies relative to massive ones (Safarzadeh & Scannapieco 2017).

Interestingly, the radial profile of dwarf galaxies we measured in A133 can be described by a power law with a slope close to that expected for the distribution of objects on their first infall. Indeed, the spherical infall model predicts that before shell crossing, the density profile of matter is $\rho \propto r^{-\gamma}$ with $\gamma \approx 1.5$, while we derive $\rho_{3D} \propto r^{-1.77\pm0.2}$ for faint galaxies (Section 5.1).

Notably, a similar power-law radial distribution of blue galaxies was measured in the SDSS (Baxter et al. 2017) and the DES clusters (Shin et al. 2019). Given the expectation for the power-law profile of infalling population of matter and galaxies, the most straightforward interpretation of this result is that galaxies do not remain blue much beyond the first pericenter passage and that the population of blue galaxies is thus dominated by infalling galaxies on their first approach to the pericenter, as was previously suggested for dwarf galaxy populations in Fornax (Drinkwater et al. 2001) and Virgo (Conselice et al. 2001) clusters. Physically, this can happen if star formation of galaxies is decreased and their color reddens on the timescale comparable to the cluster crossing time. The power-law distribution of dwarf galaxies we find in A133 can have a similar origin, at least partly, although the reasons for the disappearance of dwarf galaxies from the sample after the pericenter passage may be different.

Galaxies can suffer significant morphological transformations and mass loss due to tidal forces (e.g., Moore et al. 1999) that peak strongly around the orbital pericenter. For a given orbit and strength of the tidal force, stellar systems embedded in a halo with flattened central dark-matter density profile would experience stronger mass loss and can experience significant increase in the half-mass radius of the stellar distribution (Errani et al. 2015, 2017). The latter will lead to a significant decrease of the galaxy stellar surface density and surface brightness, potentially bringing it below detection limit of our observations. Thus, feedback that is expected to flatten dark-matter distribution predominantly in the centers of dwarf galaxies of $M_\star \sim 10^9$–$10^{10}\,M_\odot$ may affect dwarf and luminous galaxies very differently, thereby breaking the self-similarity of gravitational collapse. Indeed, Weinmann et al. (2011) compare results of the semi-analytic models used with cosmological simulations of clusters that match observed dwarf-to-giant galaxy ratios in Virgo, Fornax, Coma, and Perseus clusters and conclude that the tidal disruption of dwarf galaxies needs to be enhanced in the models. Observations also show indications that low surface brightness galaxies suffer significant tidal stripping and disruption in the central regions of clusters (e.g., Wittmann et al. 2017).

Another interesting fact is that in group-scale halos, the dwarf-to-giant ratio appears to be enhanced compared to the field (Zabludoff & Mulchaey 2000)—the trend opposite to that found in massive clusters, and which is reflected in the systematic change of the shape of the luminosity function from rich clusters to groups (Lan et al. 2016). This trend can be understood as a net result of two opposing trends: the increased efficiency of tidal disruption of dwarf galaxies in massive clusters due to stronger tides and larger rate of disruption of massive galaxies in groups due to more efficient dynamical friction.

7. Summary and Conclusions

This paper presents an analysis of deep optical-imaging observations of the galaxy cluster A133 with Magellan/IMACS. The summary of our main results is as follows:

1. The stellar-mass function of cluster member galaxies is reliably measured down to a mass limit of $M_\star = 3 \times 10^8\,M_\odot$ (≈0.1 of the LMC stellar mass). The mass function shows a clear two-component structure with an excess of $M_\star < 4 \times 10^9\,M_\odot$ galaxies over an extrapolation of the Schechter fit from higher masses. There is a background cluster ($z = 0.29$) projected on the center of A133, but based on the spatial distribution of faint galaxies, we confirm that the low-mass component is associated with A133 itself.
2. Interestingly, the radial profile of dwarf galaxies ($M_\star < 4 \times 10^8\,M_\odot$) we measured in A133 can be described by a power law with a slope of -1.77 ± 0.2.

This is close to the power-law radial distribution with the slope of ≈ -1.5 expected for objects on their first infall in the spherical infall model of cluster formation. This similarity may indicate that dwarf galaxies are disrupted efficiently in clusters and that most of them do not survive for more than a single orbit. However, additional observational measurements and more detailed modeling are required to test this conjecture.

3. We have measured an extended halo of the brightest cluster galaxy to $\sim$200 kpc. Its profile is fully within the range of BCG envelopes measured for other low-z clusters (e.g., Kravtsov et al. 2018). Including the outer envelope, the BCG contributes 33% of the cluster stellar mass within r_{500c}, also in the range of previously observed values (Gonzalez et al. 2000; Kravtsov et al. 2018; Kluge et al. 2019; Zhang et al. 2019; DeMaio et al. 2020).
4. The total stellar mass has been measured in a range of radii out to $\approx$2.5 Mpc with formal statistical uncertainties of $<15\%$. The dominant source of systematic uncertainty is the stellar mass-to-light ratio. We have used the $V - R$ color dependence of M/L from Bell et al. (2003) computed using population synthesis models and corrected to a "diet Salpeter" stellar initial mass function. For comparison, the M/L values for the Chabrier (2003) IMF would already be $\sim$25% lower. Detailed studies of the impact of the M/L assumptions on the stellar-mass measurements in A133 are beyond the scope of this paper.

This paper includes data gathered with the 6.5 m Magellan Telescopes located at Las Campanas Observatory, Chile, and public archival data from the Dark Energy Survey (DES). We are grateful to Ann Zabludoff for useful discussions related to existing observational constraints on the dwarf-to-giant galaxy trends in galaxy groups and clusters. S.S. and R.K. were supported by NASA contract NAS8-03060. A.K. was supported by the NSF grant AST-1714658 and by the Kavli Institute for Cosmological Physics at the University of Chicago through grant PHY-1125897 and an endowment from the Kavli Foundation and its founder, Fred Kavli. The work of T.C. was carried out at the Jet Propulsion Laboratory, California Institute of Technology, under a contract with NASA.

Appendix A
WVDECOMP Overview and Empirical Noise Maps

WVDECOMP is the wavelet-based algorithm for finding statistically significant structures in astronomical images and separating them into a range of spatial scales of interest.[12] For full reference, see Vikhlinin et al. (1998). Here, we review the outputs produced by WVDECOMP and explain how these were used to compute spatially dependent noise maps (Section 3.3.1).

The procedure is illustrated in Figure 16. The first run of WVDECOMP over the input flat-fielded and background-subtracted image (shown in panel (a)) uses an approximate noise map, computed from the mean rms deviations over the full image area and only corrected for exposure variations. One of the outputs of WVDECOMP is the image containing identified statistically significant structures (in this case, on spatial scales $\sim 0\farcs2$–$7''$; see panel (b)). An equivalent image at the end of this procedure can be used to identify sources simply by finding local maxima in this WVDECOMP output, as shown in Figure 3 above. This image can also be used to identify "islands" of significant signals around each detected source. Such islands are useful for selecting image subsections for more detailed modeling and for masking out unrelated sources. Identification of the islands is straightforward for isolated sources. In the case of the overlapping sources, a version of the "water fill" algorithm can be used (He et al. 2013). A similar algorithm is used for source de-blending in *SExtrator* (Bertin & Arnouts 1996).

Here, we use the WVDECOMP output to compute the source-cleaned image that retains all of the noise (panel (c)). A convolution of this source-free image with a wide Gaussian (panel (d)) gives an estimate of the local background (see Section 3.2). Note a slight enhancement of the estimated background at the position of a brighter elliptical galaxy near a top-right corner of the image. This enhancement is insignificant in this case, but becomes a problem for the brightest galaxies and the cluster BCG, in which cases we used the global background (Section 3.3.2). A convolution of the same source-free image with the WVDECOMP's wavelet kernel, which is then squared, appropriately renormalized, and smoothed with a $\sigma = 3''$ Gaussian, provides an estimate of the spatially variable noise (panel (f)). This map serves as an input to the final run of WVDECOMP leading to source detections (see Figure 3 for comparison).

[12] WVDECOMP is available at an online repository archived at doi:10.5281/zenodo.3610345.

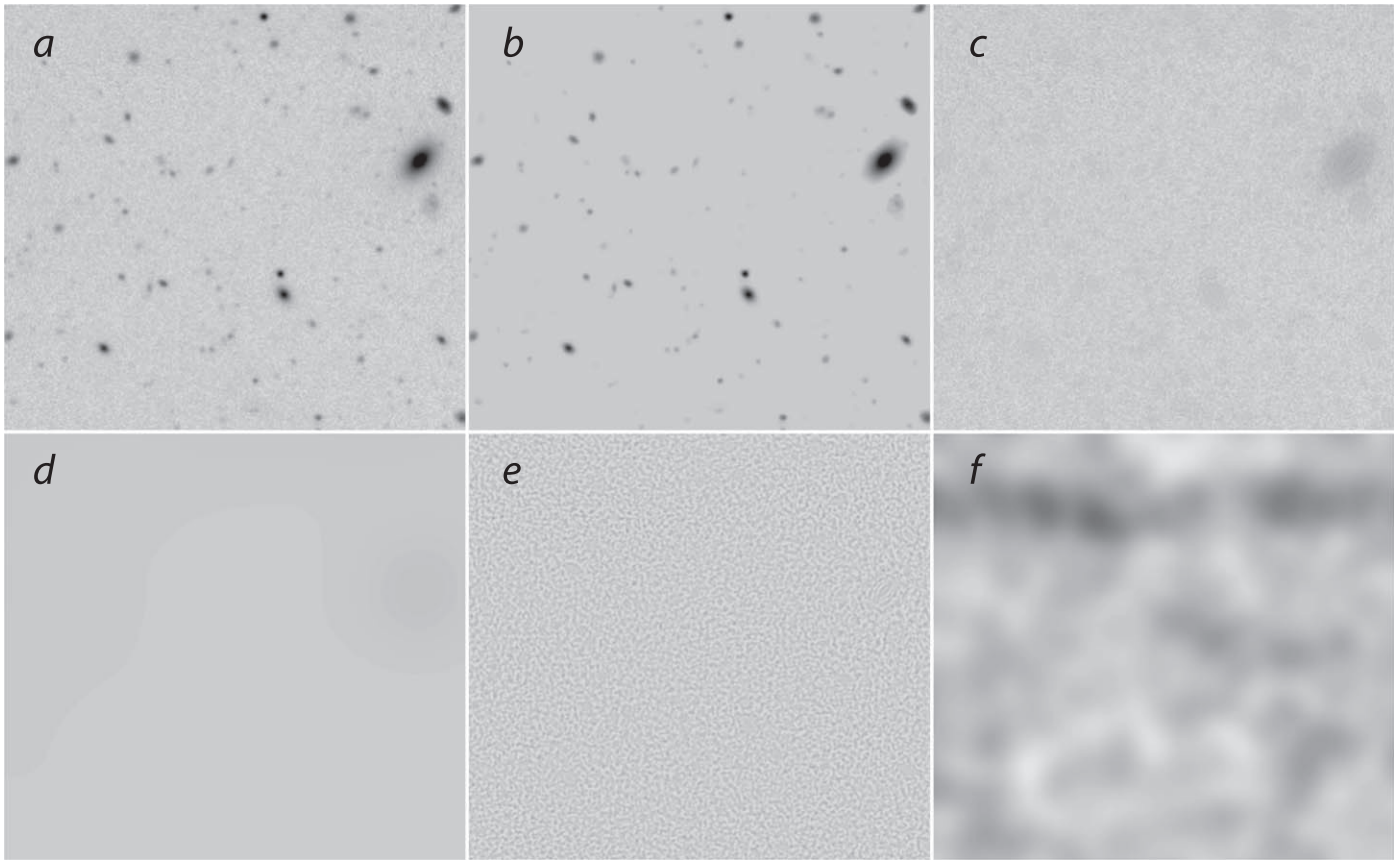

Figure 16. Steps in making the spatially nonuniform noise maps for source detection. The flat-fielded, background-subtracted image (panel (a)) and a first-iteration noise map (see the text) serve as inputs to the initial run of WVDECOMP. The output (panel (b)) is detected structures on spatial scales $\sim 0\farcs2$–$7''$; this map has a value of 0 outside of the "islands" defined by detected structures. Panel (c) is the source-cleaned image, obtained as a difference of maps in panels (a) and (b). Panel (d) is the convolution of data in panel (c) with a Gaussian of $\sigma = 25''$; this served as the local background map (see Section 3.2). Panel (e) is the convolution of data in panel (c) with the WVDECOMP kernel on the $0\farcs4$ spatial scale. It is an estimate of pixel-to-pixel noise in the original image, modulo a renormalization factor of 0.20066. Panel (f) is the final noise map obtained by smoothing the square of the data in panel (e) with a Gaussian kernel with $\sigma = 3''$.

Appendix B
Comparison of Stellar Masses Derived from Magellan and DES Data

In order to ensure the reliability of our measured galaxy masses, we compared them with masses derived from photometric data of the Dark Energy Survey (Data release 1; DES Collaboration 2018). We selected the DES sources around the A133 BCG position and matched with our catalog in the central cluster field. Our sources belong to the red sequence and are considered to be cluster galaxies. The DES did not observe in *V*; therefore, we used the *g* filter instead. We converted DES *g* and *r* magnitudes into *sdss* magnitudes, applied the *K*-correction, and transformed magnitudes to luminosities and then to masses using Bell et al. (2003) expressions. Derived DES masses and our measured masses from the Magellan data are plotted in the Figure 17. Outliers with overestimated DES masses are located near the BCG and a bright galaxy, or parts of double sources.

We have repeated the entire analysis chain presented in this paper using DES catalogs. The DES data are shallower but cover the entire cluster region. The stellar-mass functions and the mass profiles derived from DES are fully consistent with our measurements (Figure 18). We could not use DES data for fitting the outer envelope of the BCG because of the over-subtraction of the background in the publically available DES

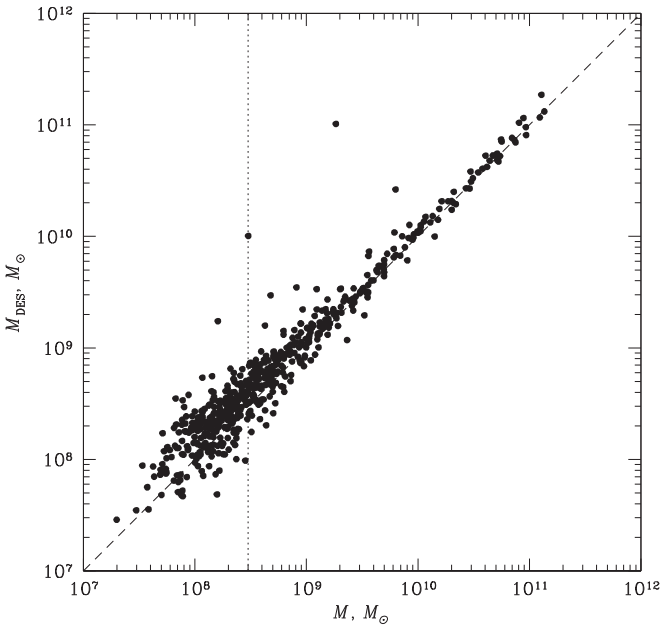

Figure 17. Comparison of galaxy stellar-mass measurements from this study and those based on the DES photometries. The black dotted line indicates our adapted lower mass limit of $3 \times 10^8\ M_\odot$ (Section 4).

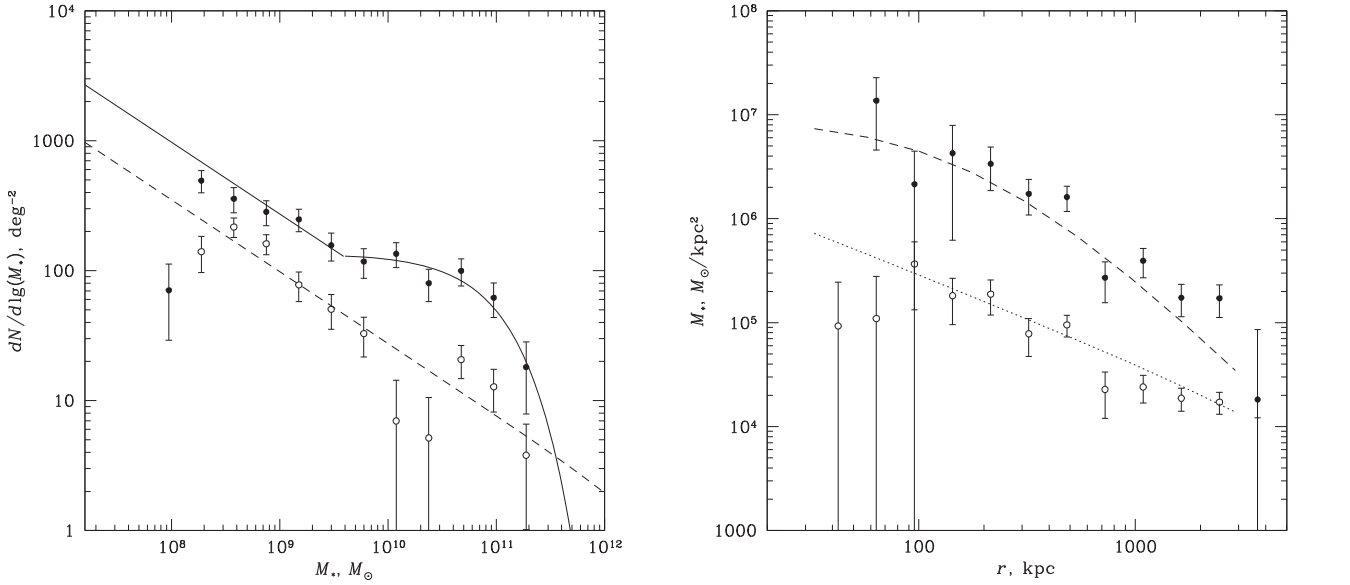

Figure 18. Stellar-mass functions and the projected mass profiles for non-central galaxies derived from the DES data. This figure presents data in the same manner as Figures 10 and 11. The lines show analytical fits to our Magellan data. Completeness of the mass function is reached at a higher threshold compared to Magellan data, so we used the mass range $M_\star = (6\text{–}40) \times 10^8\,M_\odot$ for the "faint galaxies" profile shown in the right panel. A somewhat lower normalization of this profile relative to the Magellan fit is fully consistent with the difference in the incompleteness corrections (see Section 4.2), 1.74 vs. 1.45 for the $M_\star = (3\text{–}40) \times 10^8\,M_\odot$ mass range we used for Magellan data.

images. Using DES results for non-central galaxies and our BCG profile, we obtain a total stellar mass $M_\star = (20.1 \pm 3.7) \times 10^{11}\,M_\odot$, $(31.6 \pm 5.8) \times 10^{11}\,M_\odot$, and $(40.8 \pm 6.4) \times 10^{11}\,M_\odot$ at $r = 0.5$, 1, and $1.5\,r_{500c}$, respectively, in good agreement with our values reported in Table 1.

ORCID iDs

A. Vikhlinin https://orcid.org/0000-0001-8121-0234
A. Kravtsov https://orcid.org/0000-0003-4307-634X
R. Kraft https://orcid.org/0000-0002-0765-0511
T. Connor https://orcid.org/0000-0002-7898-7664
D. Nagai https://orcid.org/0000-0002-6766-5942

References

Agulli, I., Aguerri, J. A. L., Sánchez-Janssen, R., et al. 2014, MNRAS, 444, L34
Allen, S. W., Evrard, A. E., & Mantz, A. B. 2011, ARA&A, 49, 409
Andreon, S. 2015, A&A, 575, A108
Bahé, Y. M., Barnes, D. J., Dalla Vecchia, C., et al. 2017, MNRAS, 470, 4186
Barkhouse, W. A., Yee, H. K. C., & López-Cruz, O. 2007, ApJ, 671, 1471
Barkhouse, W. A., Yee, H. K. C., & López-Cruz, O. 2009, ApJ, 703, 2024
Barnes, D. J., Kay, S. T., Bahé, Y. M., et al. 2017, MNRAS, 471, 1088
Battaglia, N., Bond, J. R., Pfrommer, C., & Sievers, J. L. 2013, ApJ, 777, 123
Baxter, E., Chang, C., Jain, B., et al. 2017, ApJ, 841, 18
Bell, E. F., McIntosh, D. H., Katz, N., & Weinberg, M. D. 2003, ApJS, 149, 289
Bellstedt, S., Forbes, D. A., Romanowsky, A. J., et al. 2018, MNRAS, 476, 4543
Bennett, C. L., Larson, D., Weiland, J. L., & Hinshaw, G. 2014, ApJ, 794, 135
Bertin, E., & Arnouts, S. 1996, A&AS, 117, 393
Binney, J., & Merrifield, M. 1998, Galactic Astronomy (Princeton, NJ: Princeton Univ. Press)
Bower, R. G., Lucey, J. R., & Ellis, R. S. 1992a, MNRAS, 254, 601
Bower, R. G., Lucey, J. R., & Ellis, R. S. 1992b, MNRAS, 254, 589
Budzynski, J. M., Koposov, S. E., McCarthy, I. G., & Belokurov, V. 2014, MNRAS, 437, 1362
Budzynski, J. M., Koposov, S. E., McCarthy, I. G., McGee, S. L., & Belokurov, V. 2012, MNRAS, 423, 104
Bullock, J. S., & Boylan-Kolchin, M. 2017, ARA&A, 55, 343
Busch, P., & White, S. D. M. 2017, MNRAS, 470, 4767
Chabrier, G. 2003, PASP, 115, 763
Chilingarian, I. V., Melchior, A.-L., & Zolotukhin, I. Y. 2010, MNRAS, 405, 1409
Chilingarian, I. V., & Zolotukhin, I. Y. 2012, MNRAS, 419, 1727
Connor, T., Kelson, D. D., Donahue, M., & Moustakas, J. 2019a, ApJ, 875, 16
Connor, T., Kelson, D. D., Mulchaey, J., et al. 2018, ApJ, 867, 25
Connor, T., Zahedy, F. S., Chen, H.-W., et al. 2019b, ApJL, 884, L20
Conselice, C. J., Gallagher, J. S. I., & Wyse, R. F. G. 2001, ApJ, 559, 791
Cui, W., Knebe, A., Yepes, G., et al. 2018, MNRAS, 480, 2898
DeMaio, T., Gonzalez, A. H., Zabludoff, A., et al. 2018, MNRAS, 474, 3009
DeMaio, T., Gonzalez, A. H., Zabludoff, A., et al. 2020, MNRAS, 491, 3751
DES Collaboration 2018, ApJS, 239, 18
Diemer, B., & Kravtsov, A. V. 2014, ApJ, 789, 1
Dressler, A., Bigelow, B., Hare, T., et al. 2011, PASP, 123, 288
Drinkwater, M. J., Gregg, M. D., & Colless, M. 2001, ApJL, 548, L139
Driver, S. P., Phillipps, S., Davies, J. I., Morgan, I., & Disney, M. J. 1994, MNRAS, 268, 393
D'Souza, R., Kauffman, G., Wang, J., & Vegetti, S. 2014, MNRAS, 443, 1433
Eckert, D., Ettori, S., Coupon, J., et al. 2016, A&A, 592, A12
Errani, R., Peñarrubia, J., Laporte, C. F. P., & Gómez, F. A. 2017, MNRAS, 465, L59
Errani, R., Peñarrubia, J., & Tormen, G. 2015, MNRAS, 449, L46
Frenk, C. S., White, S. D. M., Bode, P., et al. 1999, ApJ, 525, 554
Gladders, M. D., López-Cruz, O., Yee, H. K. C., & Kodama, T. 1998, ApJ, 501, 571
Gonzalez, A. H., Sivanandam, S., Zabludoff, A. I., & Zaritsky, D. 2013, ApJ, 778, 14
Gonzalez, A. H., Zabludoff, A. I., Zaritsky, D., & Dalcanton, J. J. 2000, ApJ, 536, 561
Han, J., Cole, S., Frenk, C. S., Benitez-Llambay, A., & Helly, J. 2018, MNRAS, 474, 604
Harsono, D., & De Propris, R. 2009, AJ, 137, 3091
He, P., Zhao, L., Zhou, S., & Niu, Z. 2013, IEEE Transactions on Wireless Communications, 12, 3637
Hellwing, W. A., Frenk, C. S., Cautun, M., et al. 2016, MNRAS, 457, 3492
Henden, N. A., Puchwein, E., Shen, S., & Sijacki, D. 2018, MNRAS, 479, 5385
Huang, S., Leauthaud, A., Greene, J. E., et al. 2018, MNRAS, 475, 3348
Kaiser, N. 1984, ApJL, 284, L9
Kausch, W., Gitti, M., Erben, T., & Schindler, S. 2007, A&A, 471, 31
Kay, S. T., Thomas, P. A., Jenkins, A., & Pearce, F. R. 2004, MNRAS, 355, 1091
Kluge, M., Neureiter, B., Riffeser, A., et al. 2019, arXiv:1908.08544
Koester, B. P., McKay, T. A., Annis, J., et al. 2007, ApJ, 660, 221
Kravtsov, A. V. 2013, ApJL, 764, L31

Kravtsov, A. V., Berlind, A. A., Wechsler, R. H., et al. 2004, ApJ, 609, 35
Kravtsov, A. V., & Borgani, S. 2012, ARA&A, 50, 353
Kravtsov, A. V., Klypin, A. A., Bullock, J. S., & Primack, J. R. 1998, ApJ, 502, 48
Kravtsov, A. V., Nagai, D., & Vikhlinin, A. A. 2005, ApJ, 625, 588
Kravtsov, A. V., Vikhlinin, A. A., & Meshcheryakov, A. V. 2018, AstL, 44, 8
La Barbera, F., De Carvalho, R. R., De La Rosa, I. G., et al. 2010, AJ, 140, 1528
Lan, T.-W., Ménard, B., & Mo, H. 2016, MNRAS, 459, 3998
Landolt, A. U. 1992, AJ, 104, 340
Lang, D., Hogg, D. W., Mierle, K., Blanton, M., & Roweis, S. 2010, AJ, 139, 1782
Lauer, T. R., Ajhar, E. A., Byun, Y.-I., et al. 1995, AJ, 110, 2622
Lin, H., Kirshner, R. P., Shectman, S. A., et al. 1996, ApJ, 464, 60
Lin, Y.-T., Stanford, S. A., Eisenhardt, P. R. M., et al. 2012, ApJL, 745, L3
López-Cruz, O., Barkhouse, W. A., & Yee, H. K. C. 2004, ApJ, 614, 679
Martizzi, D., Hahn, O., Wu, H.-Y., et al. 2016, MNRAS, 459, 4408
Martizzi, D., Jimmy, Teyssier, R., & Moore, B. 2014, MNRAS, 443, 1500
Mashchenko, S., Wadsley, J., & Couchman, H. M. P. 2008, Sci, 319, 174
McCarthy, I. G., Schaye, J., Bird, S., & Le Brun, A. M. C. 2017, MNRAS, 465, 2936
Moore, B., Lake, G., Quinn, T., & Stadel, J. 1999, MNRAS, 304, 465
Morandi, A., & Cui, W. 2014, MNRAS, 437, 1909
Moretti, A., Bettoni, D., Poggianti, B. M., et al. 2015, A&A, 581, A11
Naab, T., & Ostriker, J. P. 2017, ARA&A, 55, 59
Nagai, D., & Kravtsov, A. V. 2005, ApJ, 618, 557
Navarro, J. F., Eke, V. R., & Frenk, C. S. 1996, MNRAS, 283, L72
Navarro, J. F., Frenk, C. S., & White, S. D. M. 1997, ApJ, 490, 493
Palmese, A., Lahav, O., Banerji, M., et al. 2016, MNRAS, 463, 1486
Papovich, C., Kawinwanichakij, L., Quadri, R. F., et al. 2018, ApJ, 854, 30
Pillepich, A., Nelson, D., Hernquist, L., et al. 2018, MNRAS, 475, 648
Planelles, S., Borgani, S., Dolag, K., et al. 2013, MNRAS, 431, 1487
Poggianti, B. M. 1997, A&AS, 122, 399
Pontzen, A., & Governato, F. 2012, MNRAS, 421, 3464
Randall, S. W., Clarke, T. E., Nulsen, P. E. J., et al. 2010, ApJ, 722, 825
Rines, K., & Geller, M. J. 2008, AJ, 135, 1837
Rykoff, E. S., Rozo, E., Busha, M. T., et al. 2014, ApJ, 785, 104
Safarzadeh, M., & Scannapieco, E. 2017, ApJ, 850, 99
Sánchez-Janssen, R., Aguerri, J. A. L., & Muñoz-Tuñón, C. 2008, ApJL, 679, L77
Schechter, P. 1976, ApJ, 203, 297
Schlegel, D. J., Finkbeiner, D. P., & Davis, M. 1998, ApJ, 500, 525
Shin, T., Adhikari, S., Baxter, E. J., et al. 2019, MNRAS, 487, 2900
Smith, R. M., Driver, S. P., & Phillipps, S. 1997, MNRAS, 287, 415
Somerville, R. S., & Davé, R. 2015, ARA&A, 53, 51
Sun, M., Donahue, M., & Voit, G. M. 2007, ApJ, 671, 190
Sun, M., & Vikhlinin, A. 2005, ApJ, 621, 718
Valdarnini, R. 2003, MNRAS, 339, 1117
Valentinuzzi, T., Poggianti, B. M., Fasano, G., et al. 2011, A&A, 536, A34
van den Bosch, F. C., & Jiang, F. 2016, MNRAS, 458, 2870
van Dokkum, P., Conroy, C., Villaume, A., Brodie, J., & Romanowsky, A. J. 2017, ApJ, 841, 68
Vikhlinin, A. 2013, AAS/High Energy Astrophysics Division, 13, 401.01
Vikhlinin, A., Kravtsov, A., Forman, W., et al. 2006, ApJ, 640, 691
Vikhlinin, A., Markevitch, M., Murray, S. S., et al. 2005, ApJ, 628, 655
Vikhlinin, A., McNamara, B. R., Forman, W., et al. 1998, ApJ, 502, 558
Weinmann, S. M., Lisker, T., Guo, Q., Meyer, H. T., & Janz, J. 2011, MNRAS, 416, 1197
White, S. D. M., Navarro, J. F., Evrard, A. E., & Frenk, C. S. 1993, Natur, 366, 429
Wittmann, C., Lisker, T., Ambachew Tilahun, L., et al. 2017, MNRAS, 470, 1512
Wright, A. H., Driver, S. P., & Robotham, A. S. G. 2018, MNRAS, 480, 3491
Wright, A. H., Robotham, A. S. G., Driver, S. P., et al. 2017, MNRAS, 470, 283
Zabludoff, A. I., & Mulchaey, J. S. 2000, ApJ, 539, 136
Zhang, Y., Yanny, B., Palmese, A., et al. 2019, ApJ, 874, 165